LIMNOLOGY and OCEANOGRAPHY

ASLO

Limnol. Oceanogr. 9999, 2020, 1–22

doi: 10.1002/lno.11673

The setup and relaxation of spring upwelling in a deep, rotationally influenced lake

Derek C. Roberts,[1,2*,a] **Galen C. Egan**,[3] **Alexander L. Forrest**,[1,2] **John L. Largier**,[4] **Fabian A. Bombardelli**,[1,2] **Bernard E. Laval**,[5] **Stephen G. Monismith**,[3] **Geoffrey Schladow**[1,2]
[1]Department of Civil and Environmental Engineering, University of California, Davis, California
[2]UC Davis Tahoe Environmental Research Center, Incline Village, Nevada
[3]Department of Civil and Environmental Engineering, Stanford University, Stanford, California
[4]UC Davis Bodega Marine Laboratory, Bodega, California
[5]Department of Civil Engineering, University of British Columbia, Vancouver, British Columbia, Canada

Abstract

Strong and sustained winds can drive dramatic hydrodynamic responses in density-stratified lakes, with the associated transport and mixing impacting water quality, ecosystem function, and the stratification itself. Analytical expressions offer insight into the dynamics of stratified lakes during severe wind events. However, it can be difficult to predict the aggregate response of a natural system to the superposition of hydrodynamic phenomena in the presence of complex bathymetry and when forced by variable wind patterns. Using an array of current, temperature, and water quality measurements at the upwind shore, we detail the hydrodynamic response of deep, rotationally influenced Lake Tahoe to three strong wind events during late spring. Sustained southwesterly winds in excess of 10 m s^{-1} drove upwelling at the upwind shore (characteristic of non-rotational upwelling setup), with upward excursions of deep water exceeding 70 m for the strongest event. Hypolimnetic water, with elevated concentrations of chlorophyll *a* and nitrate, was advected toward the nearshore, but this water rapidly returned to depth with the relaxation of upwelling after the winds subsided. The relaxation of upwelling exhibited rotational influence, highlighted by an along-shore, cyclonic front characteristic of a Kelvin wave-driven coastal jet, with velocities exceeding 25 cm s^{-1}. The rotational front also produced downwelling to 100 m, transporting dissolved oxygen to depth. More complex internal wave features followed the passage of these powerful internal waves. Results emphasize the complexity of these superimposed hydrodynamic phenomena in natural systems, providing a conceptual reference for the role upwelling events may play in lake ecosystems.

Motivation

Wind is a dominant driver of lake hydrodynamics and, by extension, plays a major role in lake water quality and ecology (MacIntyre and Melack 1995). Nearshore areas may show the most striking response to wind events (Wüest and Lorke 2003; Rao and Schwab 2008). This peripheral zone sees upwelling of the coldest, deepest water during wind setup under density stratification. Following wind relaxation, the nearshore zone can become hydrodynamically chaotic as internal waves interact with lake morphometry, generating localized currents and turbulence that can drive ecologically significant fluxes from the benthos (Gloor et al. 1994) and across the pycnocline (MacIntyre and Jellison 2001). The relevance of hydrodynamics to nearshore ecology (Strayer and Findlay 2010) and the importance of nearshore ecology to the full lake ecosystem (Vander Zanden and Vadeboncoeur 2020) lend additional interest to understanding fluid flow in this complex zone.

Wind-driven upwelling has been observed in lakes globally (e.g., MacIntyre and Jellison 2001; Laval et al. 2008; Pöschke et al. 2015). However, linking the detailed, time-varying dynamics of upwelling to rapidly varying water quality patterns has proven to be elusive, particularly in the complex littoral zone. Several studies use temperature measurements to note the presence of upwelling and to infer its potential relevance to nutrient and/or oxygen fluxes (Steissberg et al. 2005; Pöschke et al. 2015). Corman et al. (2010) directly link elevated littoral nutrient concentrations to the apparent passage of an upwelling front. However, their description of the upwelling dynamics is limited to a basic pattern of nearshore cooling. Combined turbulence and nutrient profile data demonstrate a relationship between internal-wave boundary mixing and diapycnal nutrient fluxes in Mono Lake

*Correspondence: dcroberts@ucdavis.edu

Additional Supporting Information may be found in the online version of this article.

[a]San Francisco Estuary Institute, Richmond, California.

(MacIntyre and Jellison 2001). However, the discrete nature of these measurements limits interpretation of the relationship between time-varying upwelling dynamics and water quality patterns.

Analytical studies of simplified basins can offer a synoptic outline of nearshore flow patterns associated with upwelling events (e.g., Beletsky et al. 1997; Stocker and Imberger 2003; De La Fuente et al. 2008). Applied hydrodynamic models add detail to this understanding (e.g., Vidal et al. 2013; Valipour et al. 2019) and have been successfully extended to predict associated water quality impacts (e.g., Leon et al. 2012; Valipour et al. 2016). However, even comparatively high-resolution modeling descriptions of nearshore hydrodynamics are limited by bathymetric resolution, grid resolution and type, under-resolved local wind patterns, and, depending on the model formulation, hydrostatic assumptions and the ability to resolve nonlinear wave features. In combining hydrodynamic model results with data from several acoustic-Doppler current profiler deployments in Lake Geneva, Cimatoribus et al. (2018) point to the importance of these complex flow features to nearshore transport and mixing.

Building conceptual models that link complex physical processes to ecosystem function requires careful generalization to fluid flow patterns in unique lake basins under unique forcing conditions. The physical limnology literature is ripe with frameworks for delineating nondimensional thresholds for specific flow responses (e.g., Monismith 1986; Horn et al. 2001; Stocker and Imberger 2003). However, these thresholds are predicated on idealized conditions that must be translated to natural systems with caution. To this end, there is a need for studies that interpret detailed observational data in the context of generalized metrics to evaluate how these metrics might be leveraged for broader understanding of lentic systems. Ecologists may be most interested in upwelling insofar as it relates to the transport of nutrients, oxygen, or other ecologically relevant water quality constituents (e.g., Corman et al. 2010; Pöschke et al. 2015). Can the spatial extent and/or magnitude of upwelling setup be reasonably predicted without complex numerical models? Are hypolimnetic water quality constituents mixed into near-surface waters during these events? Or do they simply downwell to depth upon relaxation of the wind? Are there other hydrodynamic features associated with upwelling events that might be particularly relevant to littoral ecology? In attempting to answer these questions for a specific system, this study offers insight into important considerations when integrating upwelling dynamics into conceptual models of lake ecosystems.

Using a dense array of current, temperature, and water quality measurements focused on the upwelling-prone west shore of Lake Tahoe, we describe the setup and relaxation of three large-magnitude upwelling events during late-spring stratification conditions. These highly detailed observations are interpreted in the context of analytical models of the expected hydrodynamic responses. This study offers insight into the applicability and limitations of these metrics, describes the complex nearshore response to upwelling events in unprecedented detail, and will serve to guide studies on the potential role of upwelling in the littoral ecosystems of Lake Tahoe and other lakes of comparable scales.

Background and theory

The upwelling response in density-stratified lakes is heavily dependent on the strength and duration of wind forcing, the density stratification within the lake, and the lake size and morphometry. Dimensionless variables provide a framework for categorizing the expected response to various combinations of density-stratification and wind forcing in a given basin.

The Wedderburn number (W) describes the two-dimensional, steady-state response of a two-layer, density-stratified fluid to surface shear stress in a closed basin (Thompson and Imberger 1980):

$$W = \frac{g' h_1^2}{u_*^2 L}. \tag{1}$$

In Eq. 1, $g' = g(\rho_2 - \rho_1)/\rho_o$ is the reduced gravity term; ρ_1 and ρ_2 are the surface and bottom layer densities, respectively, ρ_o is a reference density, and g is acceleration due to gravity; h_1 is the surface layer thickness; u_* is the surface shear velocity, representing the strength of the wind; L is a characteristic length scale for the lake. The Wedderburn number is the product of the bulk Richardson number ($R_i = g' h_1 / u_*^2$), where R_i^{-1} represents the linear slope of the pycnocline, multiplied by the aspect ratio of the surface layer (h_1/L), yielding an estimate of the steady-state tilt of the pycnocline under a given set of wind and density stratification conditions. Following assumptions of linear tilt, the density interface theoretically reaches the upwind surface at $W = 0.5$, though $W = 1$ is widely used as an order-of-magnitude threshold for this "full upwelling" condition. The setup time required to reach pseudo-steady-state conditions is one-quarter of the fundamental internal seiche period (T_i) which can be calculated using the two-layer assumption, as $T_i = 2L/\sqrt{g' h_1 h_2/(h_1 + h_2)}$ (Spigel and Imberger 1980), or by considering continuous stratification, $T_i = 2L/c$, with the celerity (c) of the fundamental internal wave determined following Gill (1982). Consideration of setup time ($T_i/4$) in the preparation/filtering of wind data effectively incorporates the role of wind duration into calculations of W (Stevens and Lawrence 1997); the pycnocline tilt predicted by W can be expected to loosely represent the aggregate effect of the wind conditions over the preceding period $T_i/4$.

The Burger number,

$$S = \frac{4}{T_i f} \tag{2}$$

represents the ratio of the internal wave celerity to the influence of Earth's rotation (1982) and can be thought of as an internal wave-specific nondimensionalization of the Rossby radius ($L_r = c/f$); f is the latitude-dependent Coriolis parameter. At $S = 1$, a half-oscillation of the fundamental internal seiche is completed in the time required for the lake to turn a full rotation; at Burger numbers less than or equal to one, rotation plays a strong role in the internal wave field.

Considered in tandem, W and S can outline the baroclinic response of a lake to wind events (Stocker and Imberger 2003; de la Fuente et al. 2008). The initial formation of available potential energy due to wind-driven setup of baroclinic pressure gradients (upwelling) is described by W (Monismith 1986; Stevens and Imberger 1996). Upon relaxation of the wind, the transfer of initial basin-scale potential energy to the available-potential and kinetic energy of the internal wave field can be parametrized using S (Antenucci and Imberger 2001; Stocker and Imberger 2003), ultimately informing estimates of the degeneration of the initial available potential energy from basin-scale internal waves to higher-frequency wave forms and turbulence (Horn et al. 2001; Boegman et al. 2005; Shimizu and Imberger 2008).

In small lakes, $S \to \infty$, Coriolis effects can be ignored, and the traditional two-dimensional conceptualization of upwelling (e.g., Monismith 1986) can accurately describe the initial tilt of the density interface and subsequent internal seiching (Okely and Imberger 2007). In very large lakes, such as the Laurentian Great Lakes, the baroclinic response to wind shear is generally conceptualized as in the coastal ocean (Csanady 1977, 1982); estimates of geostrophic upwelling due to along-shore wind/currents do not require a characteristic length scale (W and S are not considered).

To our knowledge, there is no clear threshold for delineating when the setup of lake upwelling is better described by the closed-basin model (upwind upwelling, down-wind downwelling; e.g., Monismith 1986) vs. the coastal model (geostrophic upwelling; e.g., Csanady 1977). Despite the fact that its derivation ignores rotational effects, W has been widely used to parametrize the setup of the internal wave field in rotationally influenced lakes (e.g., MacIntyre et al. 2009; Antenucci et al. 2011). However, in these studies W was used as a simple approximation of the potential energy made available to the internal wave field; the validity of the closed-basin upwelling setup model was essentially ignored.

Rotational effects on upwelling setup may be limited by the relative magnitudes of the Ekman depth ($E_z = \sqrt{2\nu_V/f}$, where ν_V is the vertical eddy viscosity) and the pycnocline depth (which acts to limit the vertical extent of Ekman dynamics). In an infinitely deep and laterally unbounded system, the depth-averaged currents associated with surface-wind stress are expected to be 90° to the right of the wind direction in the northern hemisphere (Von Schwind 1980, pp. 128–130; Kundu et al. 2012). However, when the vertical influence of the wind is limited by a lakebed or a fluid density interface—that is, the ratio of E_z to a limiting depth is on the order of unity or larger—rotational effects should be less pronounced (Kämpf 2015). In those cases, the effects of horizontal barotropic pressure gradients due to boundaries perpendicular to, rather than parallel to, wind direction would likely dominate the upwelling setup process; the closed-basin setup model would better approximate the spatial extent and magnitude of upwelling setup. We assume that in lakes small enough that strong wind-fronts can generally be treated as uniform across the lake surface (implicit in W), yet large enough for baroclinic processes to be rotationally influenced under typical stratification (as approximated by S), there is superposition of both coastal/geostrophic and closed-basin effects. We herein use these limits to define "medium-sized" lakes, the focus of this study.

A considerable body of research has addressed the hydrodynamic response of density-stratified, medium-sized lakes to sustained wind events. The classical response—described in Lake Biwa (Saggio and Imberger 1998), Lake Kinneret (Marti and Imberger 2008), Mono Lake (Vidal et al. 2013), Lake Geneva (Bouffard and Lemmin 2013), and Lake Tahoe (Rueda et al. 2003), among others —evolves as follows. (1) Isotherms are depressed at the downwind side of the lake and upwelled at the upwind shore; the magnitude of this tilt can be predicted as $f(W)$. (2) The wind relaxes and potential energy stored in the tilted pycnocline (baroclinic pressure gradients) is released to the potential and kinetic energy of the internal waves; S serves to parameterize the distribution of this energy between coastally trapped cyclonic (Kelvin) waves, often a dominant feature at the lake's perimeter, and anticylonic internal seiching (Poincaré waves) which may dominate flows farther from shore. (3) Internal waves interact with the lake perimeter, dissipating energy to bottom friction and devolving into localized, nonlinear, higher-frequency internal waves and turbulence.

Diapycnal mixing, which occurs throughout these stages, complicates the application of these conceptual models that are predicated on discrete strata of constant density. If winds are sufficiently strong ($W \leq 1$) during (1), an overturning region of density inversions and intense mixing can form at the upwelling front (Monismith 1986). The resulting horizontal density gradients can drive lateral circulation independent of internal waves (Rueda and Schladow 2003; Okely and Imberger 2007), with the velocity scale of the circulation estimated as:

$$U \approx \sqrt{\alpha \Delta T g h}, \quad (3)$$

where α is the thermal expansion coefficient of water, ΔT is the horizontal temperature difference, and h is the layer thickness (Monismith et al. 1990). During (3), shear instabilities along the benthic boundary (Shimizu and Imberger 2008) and within multilayer wave forms (MacIntyre et al. 1999) can drive littoral-pelagic and/or diapycnal mixing, further complicating both localized and basin-scale flow patterns.

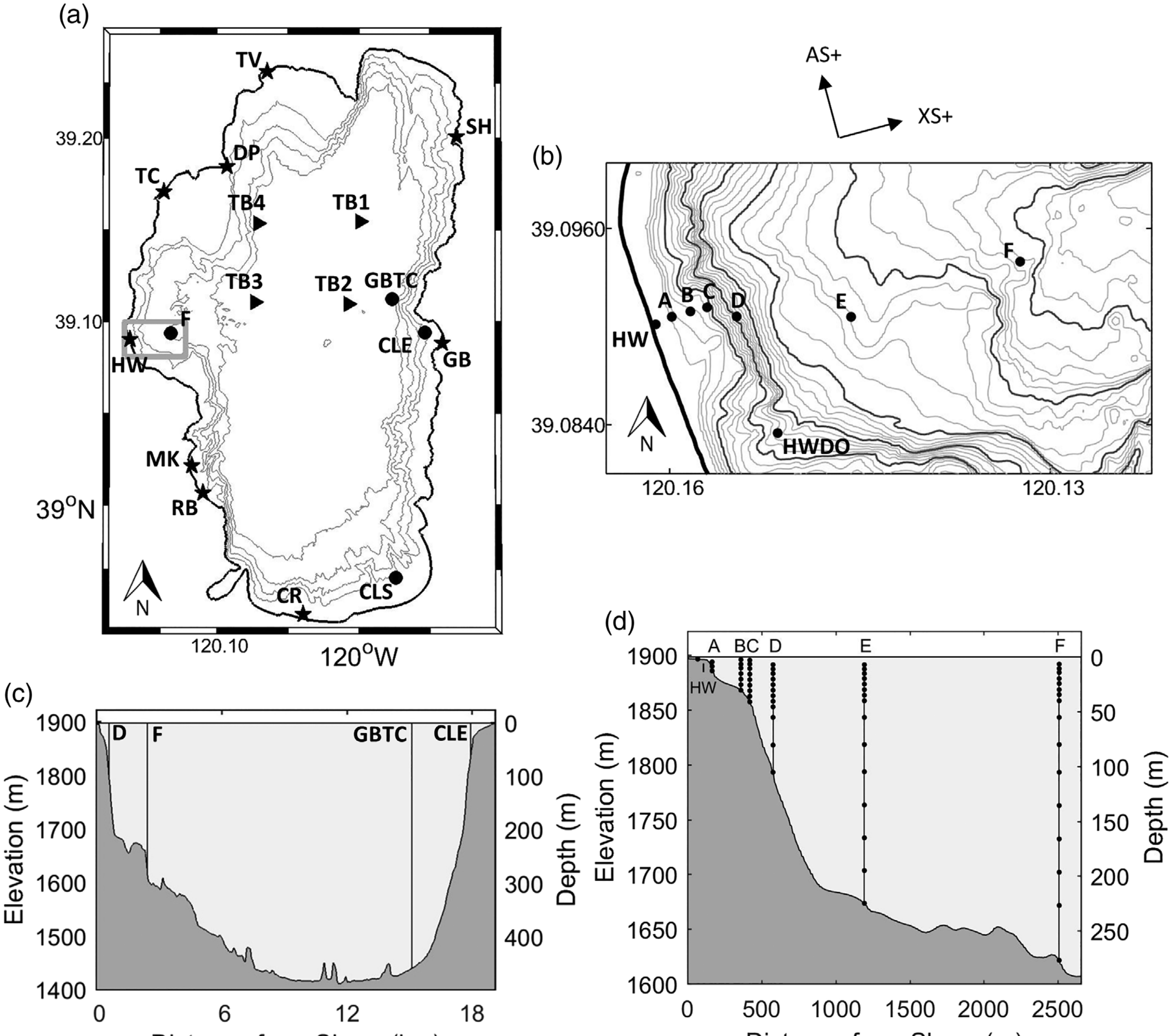

Fig. 1. Maps and profiles of instrumentation. (**a**) Bathymetric map of Lake Tahoe showing locations of nearshore stations (stars); meteorological buoys (triangles); thermistor chains (circles); and delineation of the submap focused on the west shore transect (gray box). Thin gray lines show 100-m isobaths. Note that for clarity, not all west shore transect moorings are shown. (**b**) Detailed view of the west shore transect showing locations of moorings described in Table S1. AS+ and XS+ arrows denote along-shore and cross-shore positive directions, respectively (15° offset from north). Thick and thin contour lines denote 50 m and 10 m isobaths respectively. (**c**) Bathymetric profile along a west-to-east transect from HW to GB. Vertical lines show the locations of selected moorings for reference. (**d**) Bathymetric profile along a west-to-east transect from HW through F. Vertical lines show mooring locations; dots show thermistor depths.

Methods

Study site

Lake Tahoe is a deep, oligotrophic lake on the border of California and Nevada, USA (Fig. 1a). Situated at 1897 m.a.s.l. in the Sierra Nevada mountains, the lake's hydrologic cycle is dominated by a spring snowmelt peak, typically in late May (Roberts et al. 2018). The small watershed area ($\sim$800 km^2) relative to lake volume ($\sim$156 km^3) underpins an extremely long residence time ($\sim$ 600 years), and partially explains the lake's famed clarity (average annual Secchi depth > 20 m; Swift et al. 2006). The annual mixing cycle is characterized by rapid warming during May and June, a deepening and sharpening of the thermocline through the summer and fall, and deep convective mixing in winter and early spring. However, the lake only mixes across its full depth (~ 500 m) every 3–7 years; full convective overturn is expected to become less common under a warming climate (Sahoo et al. 2016).

Both surface (Coats et al. 2008) and subsurface (Naranjo et al. 2019) watershed loading have been investigated as drivers of littoral productivity, and annual convective mixing of hypolimnetic nitrate is known to drive a peak in late-winter/early-spring primary production (Paerl et al. 1975). Observations confirm the presence of large-magnitude upwelling (Schladow et al. 2004; Steissberg et al. 2005) in Lake Tahoe. However, the nearshore dynamics and potential ecological significance of upwelling have not been investigated. Despite being large enough to be influenced by the rotation of the earth, the lake is small enough for wind fronts, typically out of the southwest, to generate spatially consistent wind patterns across the lake (Roberts et al. 2019*a*); Lake Tahoe classifies as "medium-sized" following our definition in the introduction.

Field data collection

A transect of temperature and current sensors was deployed perpendicular to the prevailing upwind shore (herein referred to as "the transect") from 1 May to 13 June 2018. This area of focus, shown by the gray box in Fig. 1a and detailed in Fig. 1b,d, and this study period were selected based on long-term observations of upwelling-induced cooling on the west shore during late-May and early-June. Combined with additional temperature measurements at the southern and eastern ends of the lake, at the cross-lake-south and cross-lake-east (CLS and CLE) moorings, respectively, this deployment supplemented extensive existing data collection infrastructure in Lake Tahoe. Sampling was performed along the transect throughout the deployment period.

Field data: Thermistor chains

Eight thermistor chains were deployed during the study period, supplementing an existing deep thermistor chain near Glenbrook (the Glenbrook thermistor chain; GBTC; Fig. 1a; Table S1). Seventy-eight thermistors (10 SBE39plus; 46 SBE56; 22 RBR SoloT) were distributed across the moorings at spacing specified in Table S1 and, for the transect, shown in Fig. 1d. All of the thermistors measured within $\pm 0.02°$C of the batch-mean in a well-mixed calibration bath prior to deployment and are specified to a resolution of $0.0001°$C or better. Thermistors were time-synced on a single computer and set to sample at a 30-s interval.

Pressure sensors (RBR SoloD) were mounted to the shallowest thermistor on each mooring to enable calculation of the time-varying depth of each thermistor. The SoloD's have a resolution of 0.001%, that is, better than 1 mm when deployed in less than 10 m of freshwater at the surface elevation of Lake Tahoe. The pressure sensors were time-synced on a single computer and set to sample at a 30-s interval. Barometric pressure measurements, collected at nearshore stations (described below), were subtracted from the raw pressure signals, and the resulting pressure values were converted to water depth assuming 1.0197 m of water per dbar.

The thermistor chain at GBTC was comprised of 18 SoloT thermistors, sampling every 30 s, at spacing specified in Table S1. Data were processed as described above, with the exception that pressure measurements were collected at the bottom of the chain using an RBR Concerto conductivity–temperature–depth unit (CTD).

Field data: Acoustic-Doppler current profilers

Acoustic-Doppler current profilers were deployed along the transect to measure three-dimensional velocity profiles (Table S1). All five current profilers were Teledyne RDI Workhorse models, with the frequency specifications shown in Table S1. At moorings A and B, the current profilers were mounted upwards-looking on weighted frames and positioned by divers for proper orientation. At mooring C, the current profiler was mounted on a gimballed frame and lowered into position; the data indicate that the gimballed frame properly oriented the current profiler upwards-looking. At moorings D and E, the current profilers were secured in downwards-looking orientations using buoyed harnesses. The sampling regime and depth range for each instrument is shown in Table S1.

Field data: Existing data collection infrastructure

Nine nearshore stations, shown as black stars in Fig. 1a, were deployed along the 2-m isobath, collecting conductivity, temperature, depth, wave height, chlorophyll *a* (Chl *a*) fluorescence, and turbidity data at a 30-s time step; see Roberts et al. (2019*a*) for detailed station specifications.

Dissolved oxygen (DO) data were collected at the bottom of the GBTC (458 m depth) using a Rinko optical DO sensor (resolution better than 0.01%) connected to the RBR Concerto CTD. An RBR XR-420 CTD and Aanderaa optode (resolution better than 0.05%) were used to measure DO at the Homewood Thermistor DO Station (HWDO) at 135 m depth near the transect.

Meteorological data were collected at a 5-min time step at each of the four TBx buoys, managed by the NASA Jet Propulsion Laboratory, shown in Fig. 1a. Each buoy is equipped with two anemometers located 4 m above the lake surface; wind speed and direction data were averaged for the two sensors on each buoy. The TBx buoys also included molded RBR thermistor strings (accuracy comparable to RBR SoloT), measuring temperature every 5 min at eight depths between 0.5 and 5.5 m (Table S1).

Field data: Sampling and profiling

Water samples were collected from discrete depths along the transect throughout the study period using a Van Dorn sampler and analyzed at the UC Davis Tahoe Environmental

Research Center (TERC) laboratory to determine concentrations of Chl *a* and nitrate (NO_3). Chl *a* concentrations were determined fluorometrically using a Turner Designs 10 AU fluorometer (calibrated with pure Chl *a* in 100% methanol) on GF/C filters containing particles collected from 100 mL of lake water (Strickland and Parsons 1969; Holm-Hansen and Riemann 1978). Nitrate concentrations were determined using a low-level hydrazine method (Kamphake et al. 1967) customized at TERC for the low nitrate concentrations found in Lake Tahoe. During sampling, an SBE 19plus CTD was used to record temperature profiles at the transect moorings as verification of the thermistor chain data.

Analytical techniques

Density profile time series were calculated from the thermistor chain data using the nonlinear equation of state (as implemented in the TEOS-10 MATLAB package; IOC et al. 2010) and assuming uniform specific conductivity. Long-term CTD profiling in Lake Tahoe shows near-uniform specific conductivity close to 94 μS cm^{-1} (unpublished data).

Calculations of integrated kinetic energy (IKE) and integrated potential energy (IPE) enable characterization of fluctuations in current and density profiles respectively (Rueda et al. 2003):

$$\mathrm{IKE}(t) = \frac{1}{2}\int_{h_a}^{h_b} \rho(h,t)\left(u^2 + v^2\right) dh, \tag{4}$$

$$\mathrm{IPE}(t) = \int_{h_a}^{h_b} \rho(h,t)\, g\, h\, dh. \tag{5}$$

Here h represents depth, with h_a and h_b representing the shallower and deeper limits of integration respectively; u and v represent the horizontal velocity components, g represents acceleration due to gravity, and $\rho(h, t)$ represents water density at a given depth and point in time. Upwelling events are registered as increases in IPE; the center of mass of the water column is shifted upwards.

We calculate the time-varying frequency content of the IKE and IPE signals using the open-source wavelet transform toolbox developed by Grinsted et al. (2004). The cross-wavelet transform between IKE and IPE signals—shared frequency power between horizontal currents and vertical density structure fluctuations—at individual sites are used to highlight the presence of periodic baroclinic flows characteristic of internal waves. Cross-wavelet transforms of intersite IPE signals are used to show the phasing, and thus propagation, of frequency-specific oscillations of the lake density profile.

In order to quantify the magnitude of upwelling and downwelling events, we define "depth origin" of water as the depth of a given water temperature in the 5-d, backwards-looking, moving-median profile at mooring F. This approach is akin to using the excursion of isotherms to calculate vertical transport, but more directly addresses the question "from what depth did this water come?" at a given measurement location.

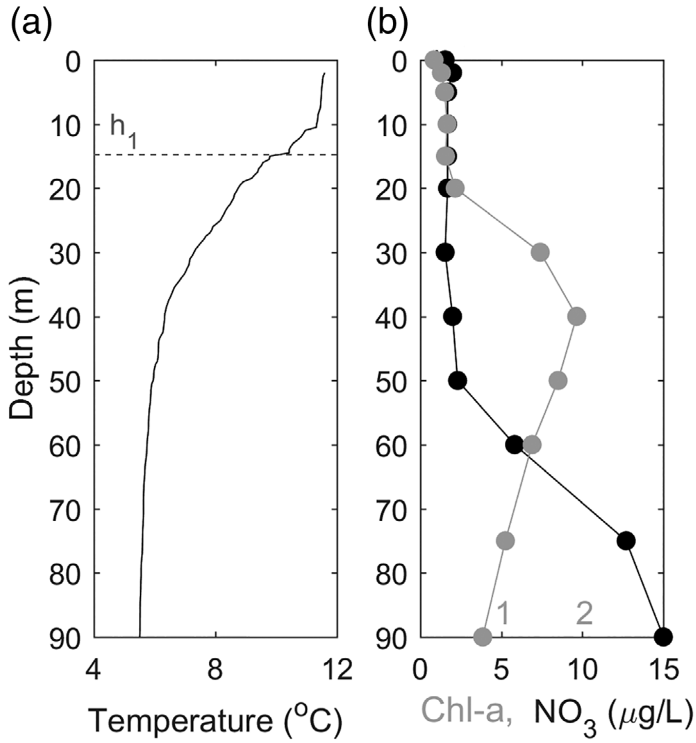

Fig. 2. Profile data collected near mooring F on 24 May 2018. (**a**) Bin-averaged temperature profile. Dashed gray line shows the approximate thermocline depth (h_1;14.95 m), defined as the depth of maximum buoyancy frequency. (**b**) Chl *a* (gray) and nitrate (black) concentrations; dots show discrete sampling depths.

Results

Pre-upwelling lake profile conditions

For the first several weeks of the experiment, calm winds and increasing solar radiation strengthened the thermal stratification of the lake. Temperature profile data from a CTD cast on 24 May (Fig. 2a) show the presence of a warmer surface layer (h_1 = 14.95 m; ρ_1 = 999.62 kg m^{-3}) overlaying cooler, denser hypolimnetic waters (ρ_2 = 1000.0 kg m^{-3}), with the separation defined by the depth of the maximum density gradient (in this case, at the 10.1°C isotherm). The average layer densities, ρ_1 and ρ_2, are calculated with consideration of the density profile and lake hypsography. Following this two-layer assumption yields an estimated fundamental internal seiche period of T_i = 48 h and Burger number S = 0.26, the latter implying significant rotational influence on the internal wave field. Consideration of continuous stratification yields T_i = 51.9 h and S = 0.24.

On the same date, nitrate concentrations were uniformly low in the surface 50 m (<2 μ L^{-1}) but increased with depth beyond 50 m (Fig. 2b). The nitricline was deeper than the

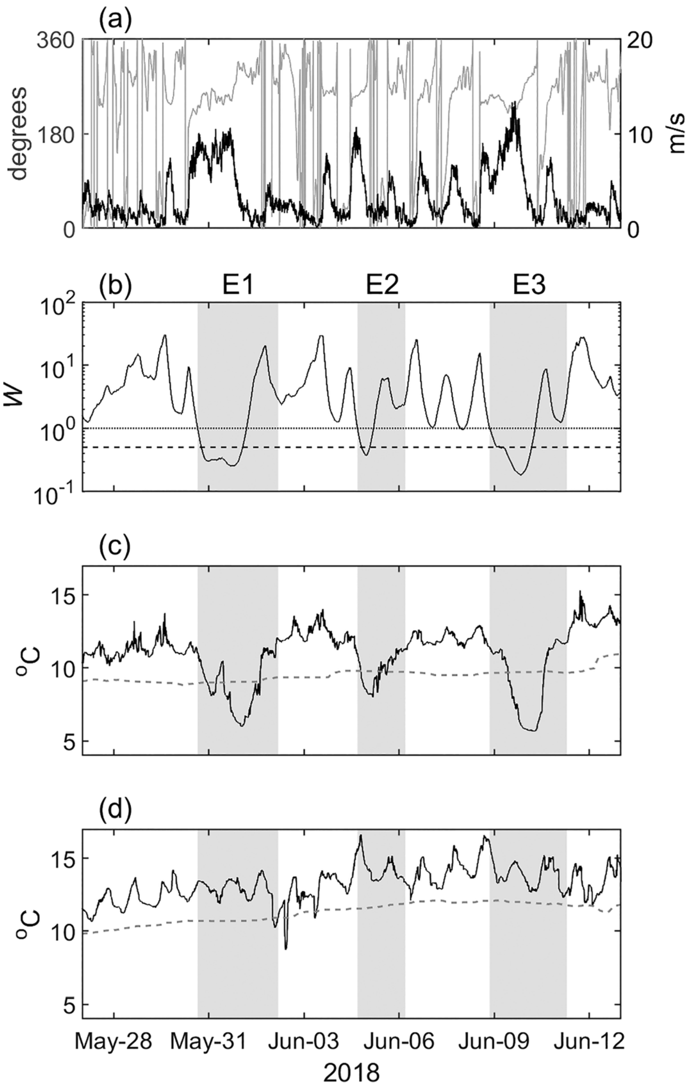

Fig. 3. Time-series windowing the three observed upwelling events, 27 May to 13 June 2018. (**a**) Wind speed (black) and wind direction (gray). (**b**) Wedderburn number (*W*). Dotted and dashed lines show 1.0 and 0.5 thresholds respectively. Gray boxes show event periods; event start is defined as the time when *W* drops below 1.0; event end is defined as 24 h after *W* rises back above 1.0. Note that values for the Lake number, which considers the continuous vertical density structure (not shown; Imberger and Patterson 1990), were virtually identical to *W*, supporting the two-layer assumption implicit in *W*. **(c)** Nearshore temperature on the west shore at HW. (**d**) Nearshore temperature on the east shore at GB. Dashed gray lines in (**c**) and **(d)** delimit 2°C below the 5-day moving-median temperature at each site.

thermocline, likely due to uptake from primary productivity at depth, made possible by light penetration through Lake Tahoe's extremely clear waters; a deep-chlorophyll maximum is present at about 40 m depth (Fig. 2b). These nitrate and Chl *a* concentration patterns are consistent with the coarser depth-resolution samples collected on 10 and 16 May at mooring D (not shown), suggesting the persistence of these vertical gradients throughout the comparatively calm first 4 weeks of May. The temperature, nitrate, and Chl *a* profiles shown in Fig. 2 are used as a reference of lake conditions preceding the highly dynamic 2-week period beginning on 30 May.

Nearshore upwelling expression

Three events with southwesterly winds exceeding 10 m s^{-1} occurred between 30 May and 10 June (Fig. 3a). Using the 24 May profile conditions to estimate h_1 and g', and a fetch length scale of 20 km (Rueda et al. 2003), a time series of W was calculated as a function of time-varying wind speed (Fig. 3b). Wind speed data were smoothed with a backwards-looking moving-average filter windowed to $T_i/4$ = 12 h so that calculated W at a given point in time is representative of the average wind forcing over the preceding upwelling setup time. The time periods of the three high-wind events are highlighted from the time at which W drops below a value of one to a time 24 h after W rises back above one. This approach brackets each event from the setup through the relaxation. Highlighted events beginning on 30 May, 4 June, and 8 June are referred to as E1, E2, and E3, respectively, as shown in Fig. 3b, with details summarized in Table 1. Since westerly/southwesterly winds dominated all three events (Fig. 3a; Table 1) "upwind shore" is synonymous with the west shore, and "downwind shore" is synonymous with the east shore.

During all three events, temperatures at the west-shore Homewood nearshore station (HW) drop well below the range of the typical diurnal fluctuations, while temperatures on the east shore at the Glenbrook nearshore station (GB) largely follow their typical diurnal pattern (Fig. 3c,d); dashed gray lines in Fig. 3c,d roughly delimit anomalous 2°C cooling below the 5-day, backwards-looking moving-median water temperature, following a similar approach by Plattner et al. (2006).

The spatial extent of upwelling expression in the nearshore is also reasonably predicted by W (Fig. 4). Approximations of the event-maximum and time-varying location of the upwelling front, as a function of W in Fig. 4a–d, respectively, are validated using temperature data from the moored thermistor

Table 1. Event summary.

Event	Start (PDT)	End (PDT)	Mean wind direction (°)	Max wind speed (m s^{-1})	Min *W*	Min HW temp (°C)
E1	30 May, 15:30	1 Jun, 4:30	244	12.9	0.26	5.98
E2	4 Jun, 16:30	5 Jun, 4:30	252	12.9	0.37	8.00
E3	8 Jun, 20:30	10 Jun, 7:00	241	17.1	0.19	5.66

chains and from nearshore stations. There is generally good agreement between observations and the W-predicted spatial extent of upwelling expression for all three events. Observations of the time-varying front location are variable, as one would expect in a natural system during a wind storm, but track the predicted magnitude and temporal patterns of tilt (Fig. 4d). For the lowest magnitude event, E2, only the farthest upwind sites saw upwelling expression, as predicted by W (Fig. 4b). For the two larger-magnitude events, E1 and E3, upwelling was present at all predicted nearshore sites, but was also unexpectedly present at Dollar Point.

Baroclinic setup

During all three events, large upward excursions of isotherms are apparent at all of the transect thermistor chains (Fig. 5a–f). During E3, near-surface temperatures dropped from about 12°C to below 6°C at all transect moorings, corresponding to vertical isotherm excursions in excess of 70 m. Excursions were large, but limited to about 50 m, during E1, when two pulses of wind over 2 days dropped near-surface temperatures below 6.2°C at moorings A–D, and below 7°C at mooring E. Perhaps due to comparatively weaker peak wind speeds, near-surface temperatures farther from shore, at mooring F, barely dropped below 8°C; the magnitude of isotherm excursions was more limited, as illustrated by the location of the predicted and measured fronts for E1 in Fig. 4a,d. Compared to events E1 and E3, isotherm excursions were less pronounced during the E2 upwelling event. Though peak wind speeds during E2 were comparable to those observed during E1 (10–11 m s^{-1}), the shorter duration of the high winds led to less extreme (higher minimum) values of W. Accordingly, transect near-surface temperatures only dropped to just below 8°C, corresponding to vertical isotherm excursions of 20–25 m at moorings A–D and more limited expression farther offshore.

At the eastern, downwind shore, near-surface temperatures remained stable during all three events (Fig. 5g,h), fluctuating by less than 1°C during the same period that temperatures were dropping by 3 – 7°C along the transect. However, the depth of the warm epilimnetic layer increased dramatically on the east shore as wind stress drove warm waters across the lake. During wind forcing, the 10.1°C isotherm descended from 15 m to approximately 30, 20, and 40 m, for events E1, E2, and E3, respectively, at both GBTC and CLE.

Figures 6, S1, and S2 detail temperature and three-dimensional current patterns at moorings B, C, D, and E for events E3, E1, and E2 respectively. During upwelling setup, when winds were the strongest, unidirectional along-shore and cross-shore current patterns do not clearly emerge, but upward vertical velocities at moorings D and E track the rise of isotherms (Figs. 6, S1, S2x-4). Isotherm patterns are illustrated by the spatially interpolated temperature profiles shown in Figs. 7 and S3, with accompanying horizontal surface-layer velocities. Broad-scale and localized current patterns appear to

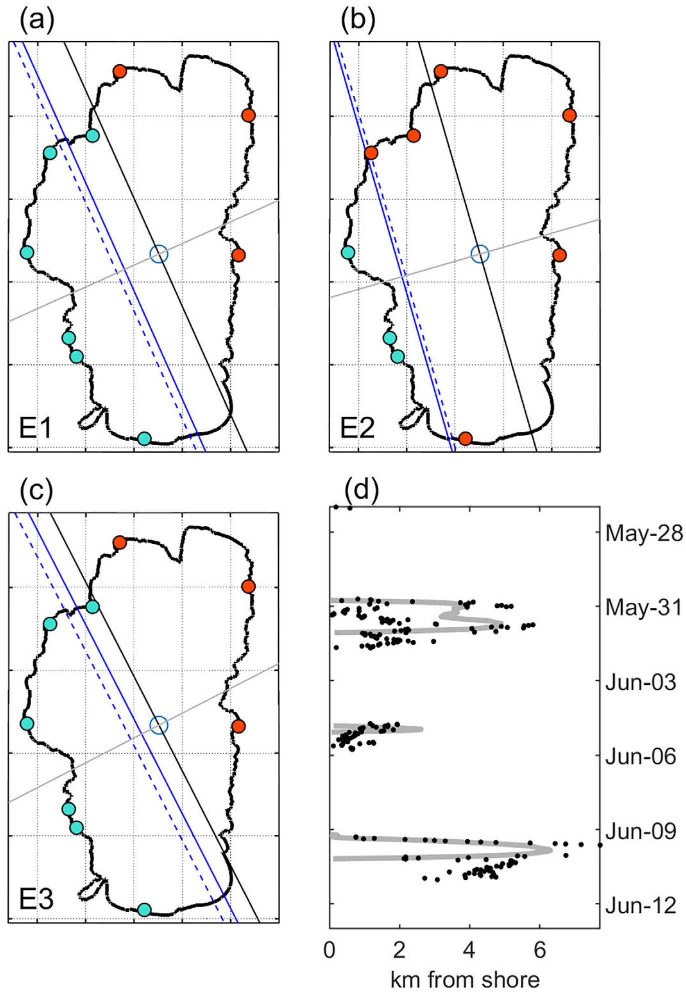

Fig. 4. Spatial extent of upwelling expression. (**a**) Estimated and measured distance from shore of upwelling front, and expression at nearshore stations, during the first wind event, E1. Gray line shows the event-mean wind direction during the event; black line shows estimated nodal line of the fundamental non-rotational seiche, defined as perpendicular to the wind and through the center of volume of the lake (blue circle). Dashed blue line shows the predicted maximum excursion of the upwelling front as a function of event-minimum Wedderburn number (W) and assumption of linear tilt. Solid blue line shows the measured maximum excursion of the upwelling front as a function of where the 10.1°C isotherm (representing the thermocline) intersected the surface based on spatially interpolated temperature profiles along the west shore transect from HW to TB3. Blue dots show nearshore stations where upwelling was observed, as defined by the simple threshold method shown in Fig. 3c,d. Orange dots show nearshore stations where upwelling was not observed. (**b**,**c**) Same as (**a**) but for the second and third events, E2 and E3, respectively. (**d**) Time-varying distance from west shore of the upwelling front. Gray line shows the estimated distance from shore as a function of W and linear assumptions. Black dots show measured distance from shore, based on spatially interpolated temperature profiles at a 30-min time step. Note that event-maximum values from (**d**) are used to define the locations of the blue solid and dashed lines in (**a–c**).

be dominated by the relaxation of upwelling and the ensuing internal wave activity (Figs. 6, 7, S1–S3).

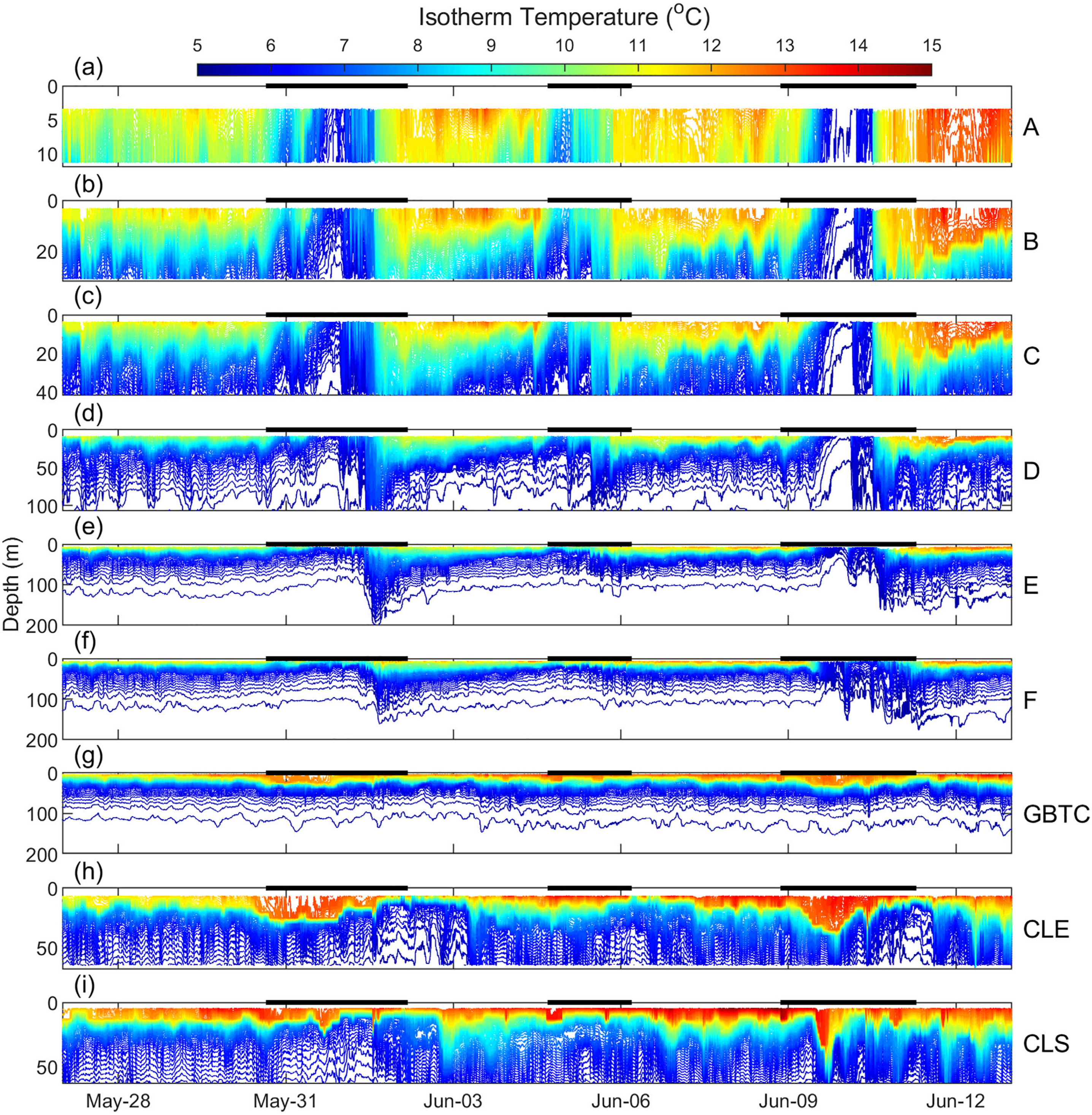

Fig. 5. Isotherm depths, at 0.1°C step, from 27 May to 13 June 2018 at (**a**) mooring A; (**b**) mooring B; (**c**) mooring C; (**d**) mooring D; (**e**) mooring E; (**f**) mooring F; (**g**) Glenbrook thermistor chain (GBTC); (**h**) mooring CLE; (**i**) mooring CLS. Thick horizontal black lines show the time periods associated with events E1, E2, and E3 as defined in Fig. 3.

Post-upwelling relaxation

Isotherm and current patterns associated with upwelling relaxation are most distinct during E3, likely due to the continuous setup (compared to E1) and large magnitude of this event; we focus on E3 in describing these patterns and use these observations to interpret comparatively less distinct patterns associated with E1 and E2.

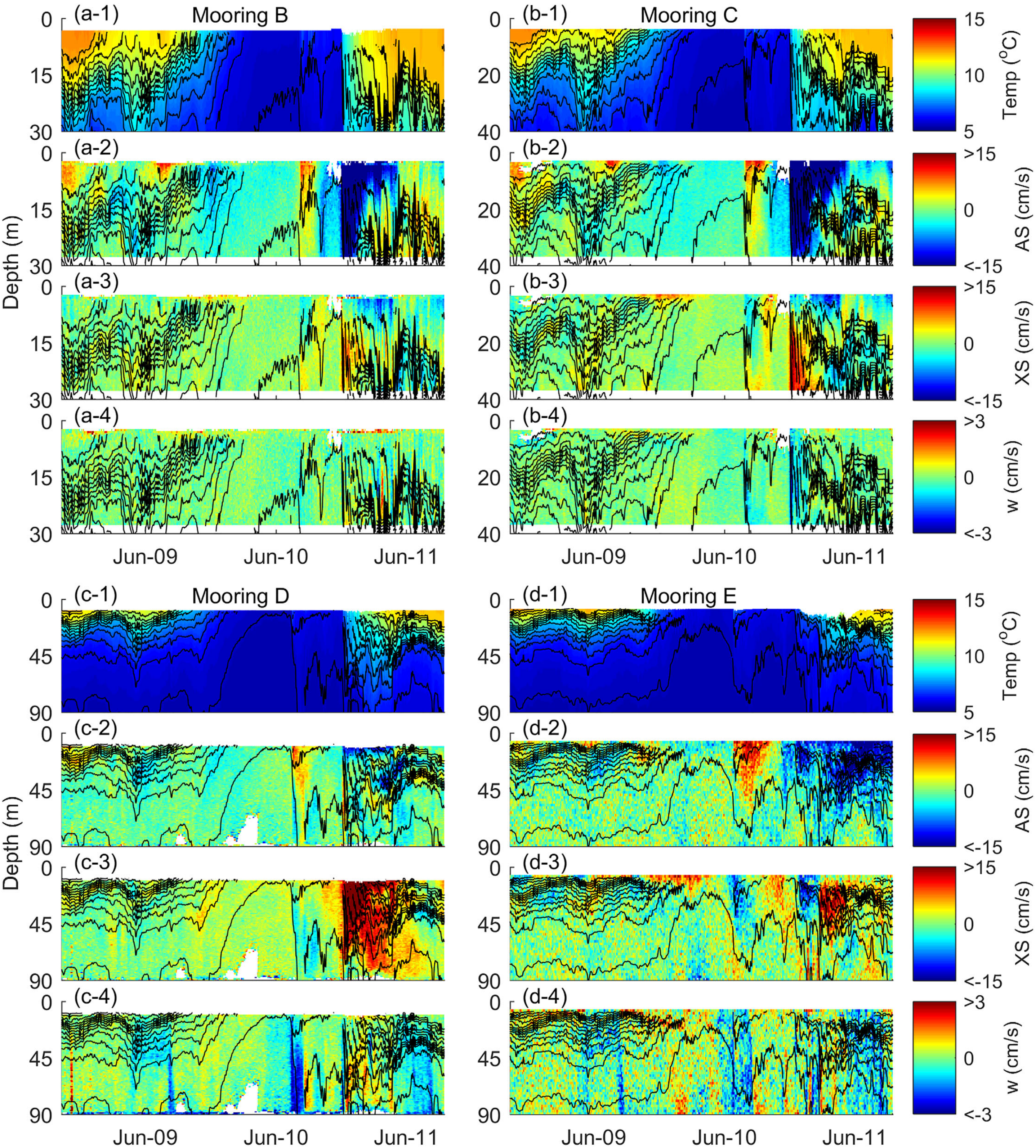

Fig. 6. Temperature and velocity contours during E3 at (**a**) mooring B; (**b**) mooring C; (**c**) mooring D; (**e**) mooring E. (**x-1**) Temperature contours with 0.5°C isotherms overlain; (**x-2**) along-shore velocity (AS) contours with 0.5°C isotherms overlain; (**x-3**) cross-shore velocity (XS) contours with 0.5°C isotherms overlain; (**x-4**) vertical velocity (**w**) contours with 0.5°C isotherms overlain.

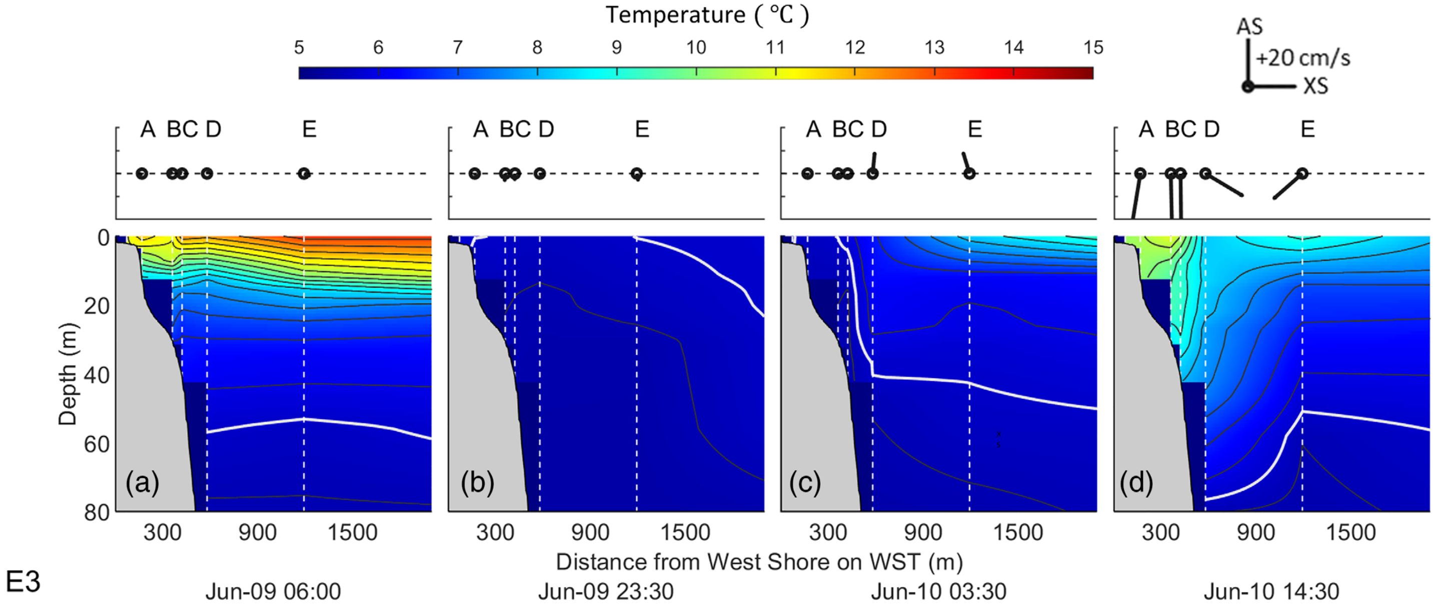

Fig. 7. Average near-surface (5–15 m depth range) horizontal velocities and spatially interpolated temperatures at snapshots in time for event E3. Black lines show 0.5°C isotherms; thicker white lines show approximate nitracline depth (5.7°C isotherm as shown at 65 m depth in Fig. 2). Dashed vertical lines shown locations of WST moorings. (**a**) Onset of wind; (**b**) upwelling setup; (**c**) initial relaxation; (**d**) passage of Kelvin wave (coastal jet).

As winds tapered toward the end of E3 late on 9 June, west shore and east shore temperatures were approximately 6°C and 13°C, respectively (Fig. 3c,d), highlighting the large baroclinic gradients associated with cross-lake differences in isotherm depths on the order of 75 m (Fig. 5). Wind relaxation was closely followed by 20–40 m downwelling (below equilibrium depth) of isotherms at the upwind shore, partially rewarming the upper water column (Fig. 6). This initial relaxation, apparent in temperature data along the transect starting around 0:00 on 10 June (Fig. 8a), is accompanied by strong downward velocities at offshore moorings D and E (Figs. 6c-4, d-4), and by toward-shore (Figs. 6x-3, 8c) and along-shore-north (Figs. 6x-2, 8c) currents. The classic surface-onshore, bottom-offshore horizontal current pattern is present at mooring E, about 1.4 km from shore (Fig. 6d-3). The northward (anticyclonic) deflection is likely due to rotational influence on the initial relaxation (Figs. 6d-2, 7c).

Figure 8a shows the approximate depth origin of water at 10 m for each of the transect moorings during E3, highlighting the timing and magnitude of isotherm excursions during the offshore-to-onshore propagation of the initial relaxation front. During E3, the front sequentially warms the water column offshore to onshore, from mooring F to mooring A, over a period of about 6 h (Fig. 8a); the velocity scale associated with frontal propagation along the transect, ~ 5 cm s^{-1}, agrees well with measured onshore currents (Figs. 6x-3, 8c). As the front arrives at each mooring, isotherms rapidly downwell 25–45 m over a 45-min period (apparent as a jump to shallower values of depth origin in Fig. 8a), representing a vertical velocity scale of 1–1.5 cm s^{-1}, in agreement with measured vertical currents (Fig. 6x-4).

Following this partial relaxation, isotherm depths remain comparatively stable for about 9 h as southerly along-shore currents increase preceding the arrival of a second front. This secondary front arrives at moorings A through D almost simultaneously (Fig. 8a; about 12:00 on 10 June), consistent with current profiler data showing dominant along-shore currents perpendicular to the transect (Figs. 6 and 7d). This along-shore front causes temperatures at 10 m along the transect to warm from onshore-to-offshore, the reverse of the initial relaxation/warming pattern (Figs. 7d, 8a).

At and inshore from mooring C, on the edge of the secondary shelf, southerly along-shore currents exceeding 20 cm s^{-1} dominate the current pattern (Figs. 6, 7d). At moorings B and C, this along-shore current is accompanied by onshore currents of ~ 5 cm s^{-1} in the surface layer and offshore currents approaching 10 cm s^{-1} at depth (Fig. 6a-3,b-3). The presence of the shallow littoral shelf at mooring A precludes layered flow structure; the southerly along-shore current dominates this nearest-to-shore signal. Strong downward velocities are present at the edge of the secondary shelf, at mooring C, and farther offshore at mooring D, but are less evident inshore. This coastal jet signal is apparent in the surface layer farther offshore, at moorings D and E, but, interestingly, offshore currents dominate the current pattern across the water column at mooring D, with a layered velocity structure emerging in the along-shore signal (Figs. 6, 8b).

The passage of this secondary alongshore front is accompanied by large, high-frequency oscillations, characteristic of

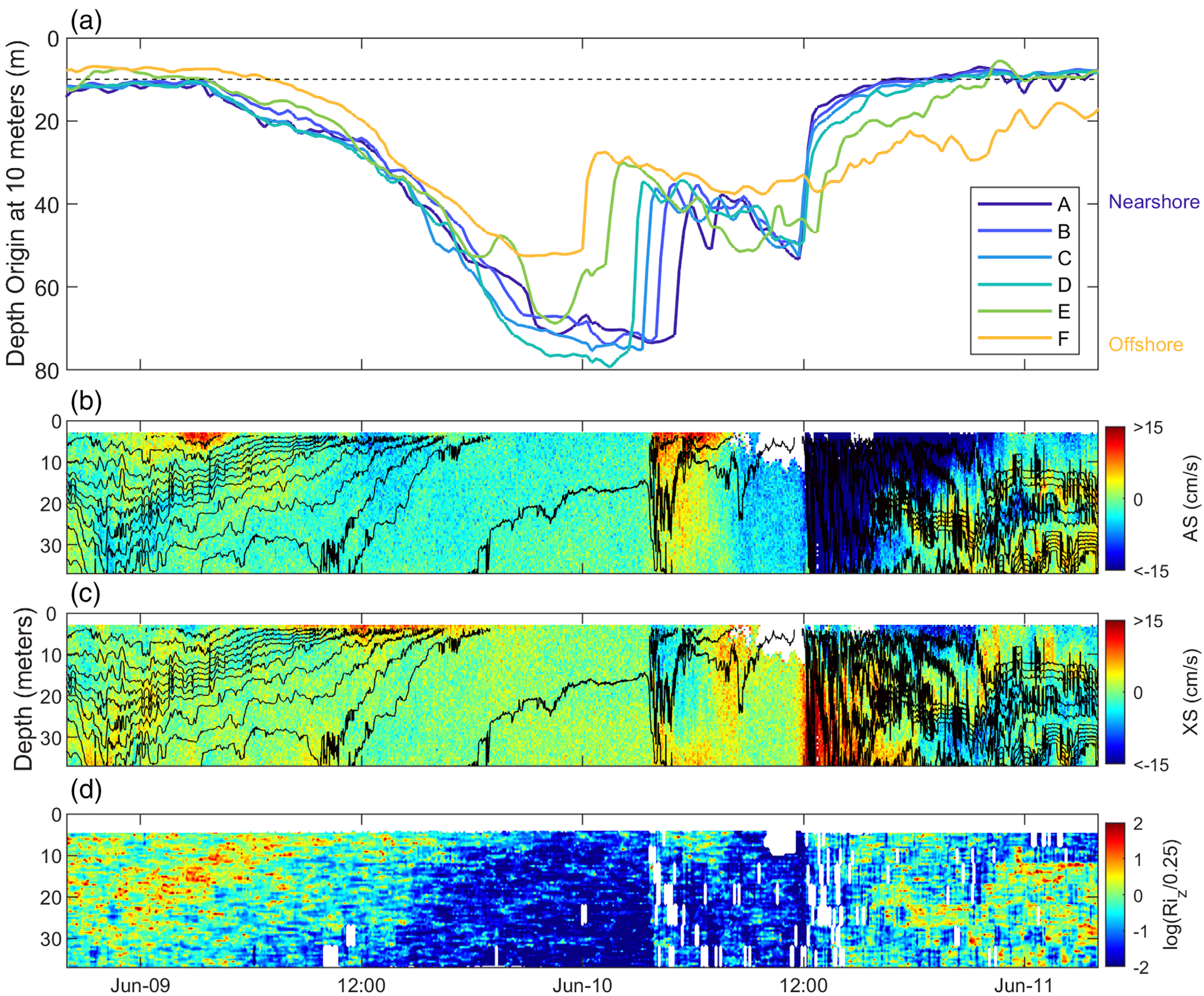

Fig. 8. Event 3: (**a**) depth-origin of water at 10-m depth at moorings A–F. depth-origin calculated as a function of 30-min time-averaged, mooring-specific temperature at 10-m depth referenced to the 5-d, moving-median, backwards-looking temperature profile at mooring F. (**b**) Along-shore velocity (positive to the north-northwest) at mooring C with 0.5°C isotherms overlaid (black lines). (**c**) Cross-shore velocity (positive to the east-northeast) at mooring C with 0.5°C isotherms overlaid (black lines). (**d**) Normalized, logarithmic gradient Richardson number (Ri_z,calculated as in Walter et al. 2016); values less than 0 ($Ri_z < 0.25$) indicate shear instabilities. Ri_z calculated using 1-h, moving-median filtered velocity data. Blank areas indicate negative vertical density gradients (instabilities) yielding nonreal values for $\log(Ri_z/0.25)$.

nonlinear internal waves (Boegman 2009), apparent in both the isotherm and vertical velocity signals (Figs. 6, 8). Offshore, at mooring E, these oscillations are on the order of 50 m, with periods of about 1 h (Fig. 6d). Similar structures are apparent inshore at mooring B at still higher frequency but more limited amplitude (Fig. 6a).

Following the passage of this secondary front, the temperature and current structure across the transect remains highly dynamic for several days. Multilayer current structures appear, closely tracking high-frequency isotherm oscillations, characteristic of higher-vertical-mode internal waves.

Shear instabilities are associated with the passage of these high-frequency oscillations, indicating the potential for diapycnal mixing (Fig. 8d). Strong vertical instabilities are present during upwelling itself, but these instabilities are driven primarily by weak density gradients in the hypolimnetic water, rather than by strong shear velocities. During the strongest currents (after 12:00 on 10 June; Fig. 8), the return of

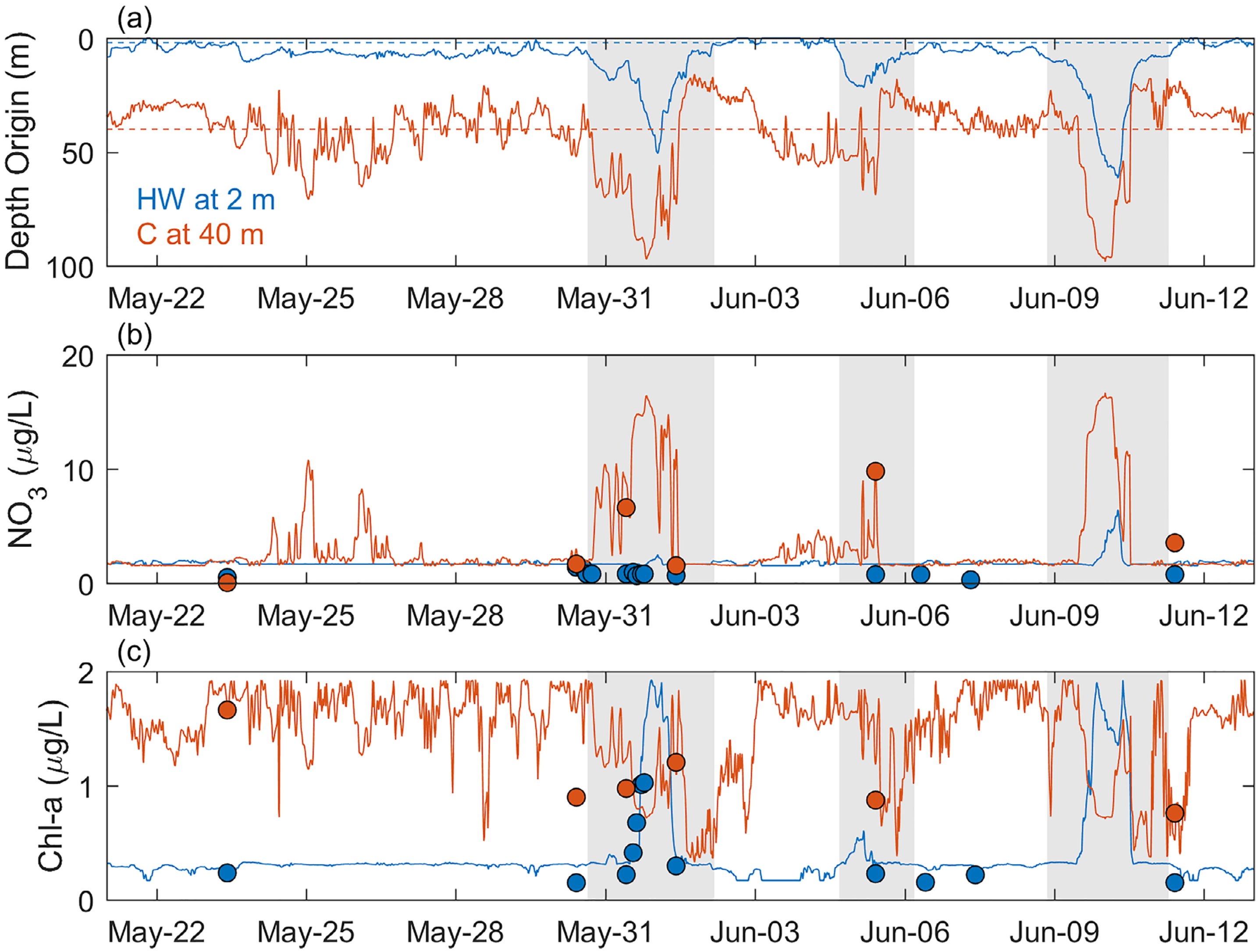

Fig. 9. Depth origin and associated concentration predictions at 2 m at HW (blue lines) and at 40 m at mooring C (red lines). Gray shading shows timing of events E1, E2, and E3 as defined in Fig. 3. (**a**) Depth origin of water as a function of 30-min time-averaged temperature referenced to the 5-d, moving-median, backwards-looking temperature profile at mooring F. Dashed lines are included for references to 2 and 40 m depths. (**b**) Predicted nitrate concentrations (lines) as a function of depth-origin of water referenced to pre-event nitrate profile shown in Fig. 2; and measured concentration values (circles). (**c**) Predicted Chl *a* concentrations (lines) as a function of depth-origin of water referenced to pre-event Chl *a* profile shown in Fig. 2; and measured concentration values (circles).

thermal stratification limits instabilities to narrower depth bands (Fig. 8d).

Relaxation patterns during events E1 and E2 are less distinct (Figs. S1–S3). The setup, partial relaxation, and then continued setup of the upwelling front during E1 (due to temporary relaxation of the winds) complicate interpretation of the associated dynamics (Fig. S1). Nevertheless, the relaxation sequence observed during E3 (Figs. 7, 8) is apparent in the temperature and current data (Fig. S3). (1) Wind relaxation is accompanied by downward vertical velocities and horizontal currents toward shore and to the north (Fig. S1); the initial warming front propagates from offshore to onshore along the transect; temperatures remain cold along the transect (compared to the east shore) as strong southerly along-shore currents build. (2) Peak along-shore currents are accompanied by rapid and near-simultaneous warming along the transect, the secondary front; along-shore currents dominate at and inshore from mooring C while strong offshore currents accompany a weaker along-shore surface current at mooring D (Fig. S1); high-frequency isotherm oscillations and vertical velocity fluctuations are present through the passage of the secondary front. (3) Layered horizontal velocity structures, characteristic of higher-vertical-mode internal waves, trail the passage of the secondary front (Fig. S1).

A comparable pattern is present through the relaxation of E2 (Figs. S2, S3b). However, the limited magnitude/spatial

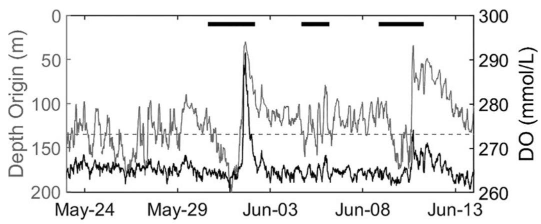

Fig. 10. Depth origin as a function of 30-min time-averaged temperature referenced to the 5-d, moving-median, backwards-looking temperature profile at mooring F (gray line) and dissolved oxygen concentration (black line) at 135 m depth (lakebed) at HWDO. Dashed gray line shows 135-m depth for reference. Thick, horizontal black lines show the time periods associated with events E1, E2, and E3 as defined in Fig. 3.

extent of the upwelling front limits interpretation of its propagation across the transect during relaxation. Interestingly, during E2, the pattern of initial cross-shore relaxation followed by secondary along-shore warming is followed by the arrival of a third front, propagating along-shore in the pattern of the secondary front (Fig. S2). This may represent the superposition of internal wave forms setup during E1.

Water quality impacts

Fluxes of water quality constituents were expected to accompany the vertical excursions of the lake strata. Using temperature as a tracer, we approximated the depth origin of water at the Homewood nearshore station and at 40-m depth at mooring C (Fig. 9a). Referencing the depth-origin timeseries to the nitrate and Chl *a* profiles from 24 May (Fig. 2b), we estimated time series of concentrations in response to vertical excursions of lake water (solid lines in Fig. 9b,c).

Through the three upwelling events, the magnitude of the upward excursions of hypolimentic water was insufficient to expect major fluxes of nitrate into the nearshore (blue line in Fig. 9b). Samples collected throughout and after E1 and E2, and shortly after E3, confirm predictions of minimal to no nitrate flux into the nearshore (blue dots in Fig. 9b). Unfortunately, no samples were collected during E3 upwelling, when the depth-origin time series predicts a nitrate concentration increase from 2 to 5 μg L^{-1} (Figs. 7c,d, 9b). At the peak of this event, elevated nitrate concentrations may have been present in the nearshore. Low nearshore nitrate concentrations measured soon after the event indicate that any upwelled nitrate was either taken up by primary producers or advected back to depth.

The upwelling amplitude was sufficient to advect deep nitrate to mid-depths. Samples collected before, during, and immediately after E1 upwelling confirm predicted nitrate fluxes to 40-m depth at mooring C (red dots and line in Fig. 9b). A sample collected mid-event during E2 similarly captured predicted advection of nitrate to mid-depths. Nitrate concentrations at 40-m appear to be slightly elevated after E3. However, the elevated value is within 1.5 μg L^{-1} of the baseline conditions.

Predictions of vertically advected Chl *a*, using the same depth-origin approach, are confirmed by measurements (Fig. 9c). Sampled data track the predicted advection of the deep chlorophyll maximum into the nearshore during E1, and the subsequent downwelling of this layer following wind relaxation (blue lines and dots in Fig. 9c). Predictions of Chl *a* concentrations at 40 m are highly dynamic (red line in Fig. 9c), due to the comparatively strong concentration gradients near this depth (Fig. 2b), introducing additional uncertainty into the predictive approach. Despite this comparatively noisy signal, predictions appear to capture the measured decreases in Chl *a* concentration associated with the advection of the deep chlorophyll maximum from its stable location at 40-m depth.

Large amplitude downwelling on the upwind shore (Fig. 5), following the relaxation of upwelling, drove warmer, more oxygen-rich water to depth (Fig. 10). Temperature measurements at 135-m depth (HWDO) register rapid increases from 5.4°C to 6.8°C and 6.5°C for events E1 and E3, respectively, corresponding to downwelling from 30 and 35 m. Rapid increases in DO concentration accompany the downwelling, but neither the DO concentrations nor the warmer temperatures persist as the density structure of the basin reequilibrates (Fig. 10).

Discussion

Upwelling setup

The Wedderburn number can be a useful tool for approximating "how large is this wind for this lake?" (Shintani et al. 2010). Addressing this question can offer insight into (1) the timing and magnitude of the upwelling of hypolimnetic water into the littoral zone; (2) upward flux of water quality constituents associated with these events; (3) the setup of available potential energy that ultimately drives current and internal wave dynamics; and (4) the structure of the post-wind dynamics, which may have an equal or larger impact on the nearshore than the upwelling itself.

In Lake Tahoe, W offers a reasonable approximation of the timing and magnitude of upwelling (Figs. 3, 4). The timing of cooling at the upwind shore is accurately predicted by W (Fig. 3). For all three events, upwind-shore temperatures generally begin to drop when W crosses below one and subsequently begin to warm when winds relax and W rises above one. Events with lower event-minimum W saw colder upwind-shore minimum temperatures (Fig. 3; Table 1), implying greater upward excursions of hypolimnetic water. The stability of downwind-shore temperatures during these periods further indicates that upwind-shore cooling is due to advection/upwelling rather than surface heat loss (Figs. 3, 4).

Care must be taken in applying this parameterization and in interpreting associated results. Reasonable agreement between estimates of T_i and S using the two-layer assumption (48 h and 0.26, respectively) and considering continuous stratification (51.9 h and 0.24, respectively) support the two-layer simplification. Given that density gradients tend to sharpen throughout the stratified season in most monomictic and dimictic lakes, the reasonable validity of this simplification during spring, when stratification tends to be more diffuse, supports the general application of W in lakes where spring estimates of T_i are similar for both two-layer and continuous stratification assumptions. In addition to requiring a two-layer assumption, application of W requires that stratification parameters (h_1, ρ_1, ρ_2) be generally representative of the basin-wide conditions. It is difficult to accurately parametrize basin-scale stratification through a set of sequential winds events because, during these highly dynamic periods, point measurements may not be representative of the basin-wide density structure (Fig. 5).

The dynamism of the internal density structure points to additional challenges associated with the application and interpretation of W. The timing of wind events with relation to the phase of pre-existing internal waves can determine whether winds "amplify" or "annihilate" existing wave energy (Antenucci and Imberger 2001; Rueda and Schladow 2003). Upwelling magnitude is highly dependent on the duration of winds relative to the baroclinic setup time, including cases where wind duration is several times longer than the setup time, and particularly for rotationally influenced systems (de la Fuente et al. 2008). Additionally, changing stratification conditions through a sequential set of events affect the theoretical setup time associated with each event.

We chose to calculate time-varying W as a function of a fixed set of stratification conditions measured prior to the three major wind events (Fig. 2a), and to use these conditions to set a fixed window ($T_i/4$ = 12 h) for low-pass filtering the wind data. The latter step was crucial to accounting for setup time. Peak winds were nearly identical for E1 and E2 (Fig. 3a; Table 1), but by incorporating the effect of longer duration winds during E1, calculations of W properly predict comparatively greater isotherm excursions during E1 (Figs. 4, 5).

Given the assumptions implicit in our parameterization, W shows remarkable predictive power through the three study events (Figs. 3, 4; Table 1). However, applying it to reconstruct long-term upwelling patterns requires an understanding of the seasonally variable time scales of change in stratification conditions. Surface temperatures quickly recovered, and even warmed, after the relaxation of upwelling (Fig. 5), likely due to the strength of the stratification and the strong solar radiation in late-May/early-June. This may have buffered residual cooling due to any dilution of hypolimnetic waters into the nearshore during upwelling and helped to maintain comparable stratification conditions at the onset of each event (Fig. 5). CTD profile data collected on 19 June (not shown) indicate a first-mode internal wave period of 46 h and S = 0.27. Both metrics are comparable to pre-event conditions. However, h_1 on 19 June was notably deeper, about 20 m, than the pre-event pycnocline depth of about 15 m. In winter, weaker density gradients, and the dramatic cooling effect of cold winds, may cause stratification conditions to change more dramatically after a single event, as observed in Lake Tahoe by Schladow et al. (2004). The effect of seasonality on the time scales over which stratification varies would need to be considered when applying W to long-term data.

Predictions of the spatial extent of upwelling expression using W may offer a useful reference but their application must be constrained. In deep lakes, where h_1 is small relative to the depth of the lake, complex bathymetry is less likely to affect the predictive power of W, which is predicated on simplifications to basin morphometry (Shintani et al. 2010). Good agreement between observed and W-predicted upwelling front location seem to confirm the applicability of W to Lake Tahoe (Fig. 4). Although the general magnitude of frontal excursions appears to be reasonably well predicted by W (Fig. 4), the true "front" is almost certainly not well represented by a straight line perpendicular to the mean wind direction; previous satellite observations of surface temperature during upwelling in Lake Tahoe confirm the presence of complex frontal patterns (Steissberg et al. 2005). The dispersion of upwelled water expected to be associated with these complex frontal patterns (Monismith 1985) may explain apparent upwelling-driven cooling at Dollar Point during E1 and E3 (Fig. 4a,c). Alternatively, limited rotational effects on northerly along-shore surface currents—that is, the superposition of coastal-style upwelling on the closed basin-style setup–could explain this observation.

Observations of upwelling at the upwind shore, rather than to the left of the wind direction, (i.e., at the north shore; Fig. 4) may be surprising given the low values of S associated with the observation period, and the clear influence of Coriolis on the resulting internal wave field. This is likely due to barotropic pressure gradients associated with the downwind shore boundary outweighing the effect of limited Ekman dynamics. Conservatively assuming $\nu_v \sim 10^{-3}$ m^2 s^{-1} in the surface layer for strong wind events (> 10 m s^{-1}; Bengtsson (1972) estimated values of about $2 \cdot 10^{-3}$ m^2 s^{-1} for winds of about 7 m s^{-1}) yields $E_z \sim 5$ m. Compared to our estimate of h_1 (Fig. 2), the ratio of E_z to the limiting depth is on the order of unity; even in a laterally unbounded space, mean surface-layer currents would not be deflected a full 90^o by the effect of Earth's rotation (Kämpf 2015). Wind-driven surface-layer currents in Lake Tahoe are likely partially deflected by the Earth's rotation, but the effect of horizontal barotropic pressure gradients due to the downwind-shore boundary, rather than leftward-shore boundary, appears to dominate the upwelling setup process. Perhaps more simply, Lake Tahoe can be considered barotropically non-rotational ($L_r = \sqrt{gH}/f >> L_{\mathrm{lake}}$; Roberts et al. 2019*b*) but baroclinically rotational ($S < 1$ and $L_r = \sqrt{g'h_1}/f << L_{\mathrm{lake}}$). Upwelling setup is fundamentally a barotropic process (with baroclinic balancing), and the relaxation has largely independent barotropic (surface seiches) and baroclinic (internal waves) modes.

Surface-offshore and deep-onshore currents classically associated with basin-style upwelling setup do not clearly emerge in the current profiler data. However, upward vertical velocities at moorings D and E track the rise of isotherms (Figs. 6, S1, S2). The absence of notable vertical velocities closer to shore, at moorings B and C, may be due to the interaction of basin-scale upwelling setup with the localized shelf feature shown in Fig. 1d; an offshore upwelling front may separate nearshore flows from the classic upwelling features that may be present farther offshore. Complex bathymetric features have been shown to limit the magnitude of upwelling as energy is instead distributed to localized internal waves and boundary mixing (MacIntyre et al. 1999; Vidal et al. 2013). The near-to-shore setup of the transect relative to the measured upwelling fronts may explain why the expected surface-offshore/deep-onshore horizontal current pattern is difficult to identify in Figs. 6, S1, and S2. The complexity of the weak horizontal currents, and their inconsistency between events, may also be a function of the sensitivity of the system to variations in wind conditions during baroclinic setup (Figs. 6, S1, S2). The short-term relaxation of the wind during E1 initiates the current pattern associated with upwelling relaxation (Fig. S1), until wind resumes, reinitiating upwelling. More limited fluctuations in wind conditions may explain smaller fluctuations in current patterns during upwelling setup for E2 and E3.

The Wedderburn number ignores the effect of rotation on upwelling setup, but its application to rotationally influenced Lake Tahoe offers reasonable predictive power (Figs. 3, 4). Perhaps this is because upwelling setup is fundamentally a response to barotropic pressure gradients, and Lake Tahoe is barotropically non-rotational. Rotation appears to play a more direct role in post-upwelling relaxation.

Post-upwelling dynamics

Following relaxation of the winds, horizontal density gradients drove the dominant currents that characterized all three events. The peak kinetic energy associated with upwelling relaxation is generally consistent with the magnitude of baroclinic setup, parametrized by W (compare peaks in Fig. S4 to minimum values of W in Table 1). This intuitive result is consistent with Stocker and Imberger's (2003) finding that surface-layer velocities scale with $W^{-1}S$. Examination of the timing of IKE peaks and of the frequency signatures of IKE and IPE throughout the events offer further insight into post-upwelling flow dynamics.

Peaks in IKE consistently occur several hours after the relaxation of the winds (Fig. S4). However, the time-lag between wind relaxation and peak IKE is inconsistent between events. This time-lag is generally negatively correlated with the event magnitude; about 6 h for E3, 10 h for E1, and 16 h for E2 (listed in order of descending event magnitude). The inconsistency in the apparent relaxation time scale would seem to imply the presence of baroclinic currents (Eq. 3) rather than basin-scale waves, since the periodicity of the latter should be independent of setup amplitude. However, defining an "event end" time is highly subjective, and the time lag is almost certainly dependent on how quickly the winds dissipate and the superposition of the event onto any existing internal wave forms.

The complex current and isotherm patterns observed during relaxation are consistent with theory, and with previous modeling results for Lake Tahoe. At the intermediate values of S observed during our study (~ 0.26), the lake is expected to support superimposed Kelvin and Poincaré waves (Antenucci and Imberger 2001; Stocker and Imberger 2003; de la Fuente et al. 2008). Observations and modeling results from Rueda et al. (2003) confirm the presence of both cyclonic (Kelvin) and anticyclonic (Poincaré) internal waves in Lake Tahoe. Those results were produced for a winter period, when the thermal profile of the lake was different than during our study period, but the counter-acting effects of weaker thermal stratification and deeper h_1 yield a similar winter value of $S = 0.24$ to our observations from spring, $S = 0.26$. Despite event-to-event variability in relaxation time scales, we expect that a comparable set of superimposed internal waves was present during our observations.

Cross-wavelet power in the IKE and IPE signals at moorings A–E confirm the presence of periodic baroclinic flows associated with the three upwelling events (Fig. 11). In particular, a $\sim$ 120-h signal is excited at the beginning of E1 and carries through to the end of the study period. This periodicity is consistent with the first-mode Kelvin wave (K1) observed by Rueda et al. (2003) for a similar Burger number. The timing of the three wind events, spaced by about 100–130 h, lends the possibility that the periodic signal is related to the forcing rather than to a resonant internal wave. However, the phasing of the cross-wavelet power in the IPE signals between mooring D and moorings CLS and CLE indicate cyclonic propagation consistent with a Kelvin wave; the K1 IKE signal at mooring D leads the signals at CLS and CLE by about 90° and 180°, respectively (Fig. S5). The post-upwelling, southerly along-shore currents at moorings A–C (Figs. 6, S1, S2) are consistent with the expected expression of a Kelvin wave as a cyclonic "coastal jet" (Antenucci 2009), a phenomenon observed in other rotationally influenced lakes (e.g., Beletsky et al. 1997; Valipour et al. 2019).

The initial front, toward-shore and northerly surface currents observed immediately after wind relaxation, appears to be consistent with rotational influence on the relaxation of the initial tilt (e.g., E3 as illustrated in Figs. 6–8), characteristic of a Poincaré wave. The first wind event, E1, excited a 48-h signal (Fig. 11), which is consistent with the estimate of the fundamental internal seiche period (T_i = 48 hours) and, accordingly, with the expected period of the first-mode Poincaré wave. The second event, E2, appears to destroy this signal (gaps in the 48-h cross-wavelet power during E2 winds in Fig. 11), perhaps due to the superposition of antecedent internal waves, excited during E1 or during the weaker wind event that preceded E2 by 1 d. The two pulses of along-shore

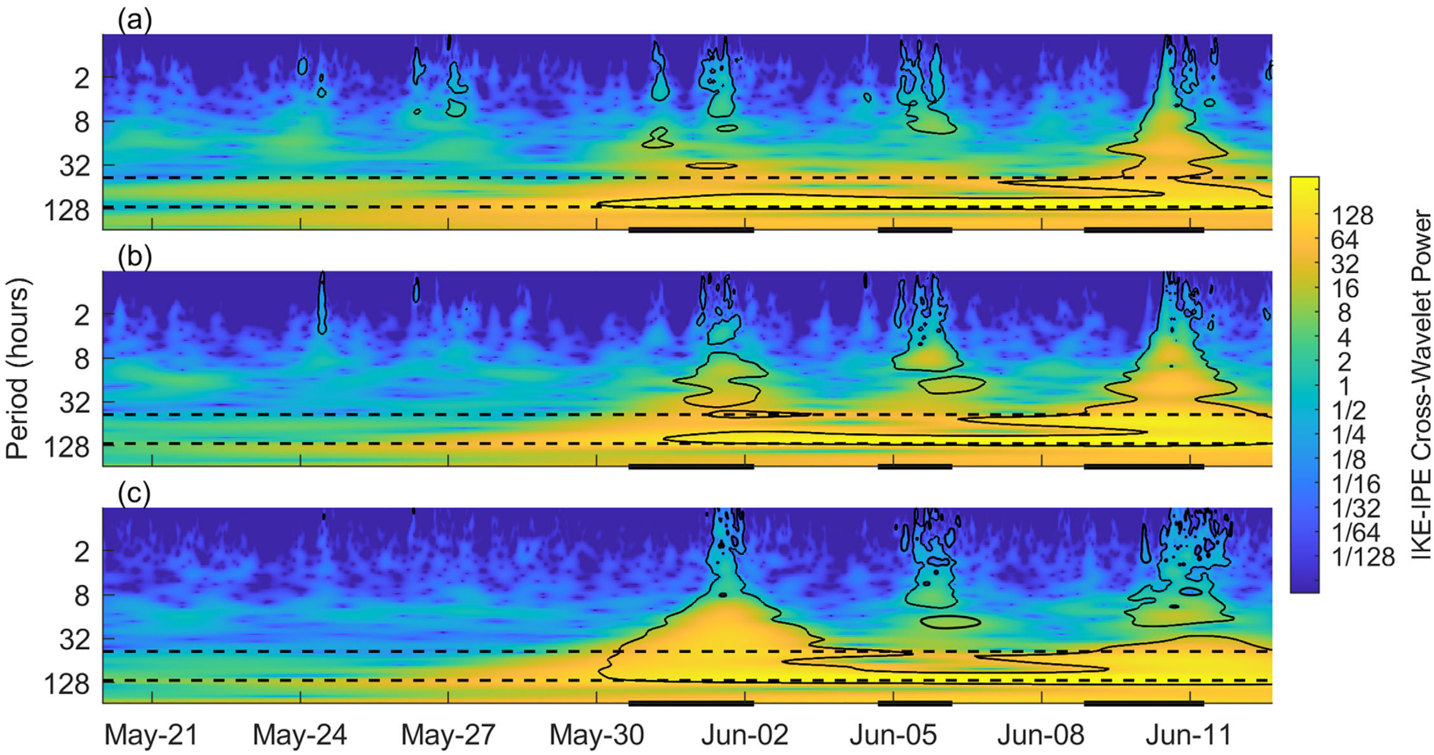

Fig. 11. Cross-wavelet power between IKE and IPE, calculated across the full mooring extent at moorings: (**a**) A; (**b**) C; (**c**) E. Warm colors indicate shared periodic signals in the IKE and IPE time series at a given time for a given frequency range. Black lines delineate areas of greater than 95% confidence. Dashed black lines highlight the 48- and 120-h bands. Thick black lines show the time periods associated with events E1, E2, and E3 as defined in Fig. 3.

currents following E2 winds (Fig. S2) offer further evidence of the overlapping effects of sequential wind events. These superimposed features may also be present during E1 and E3 but could be drowned out by the large-amplitude, along-shore fronts during these larger magnitude events.

A broad spectrum of higher-frequency internal waves is excited during upwelling relaxation, particularly for the most energetic event, E3 (Fig. 11). This result is consistent with observations of rapid isotherm oscillations during and following the passage of the Kelvin wave front and with similar

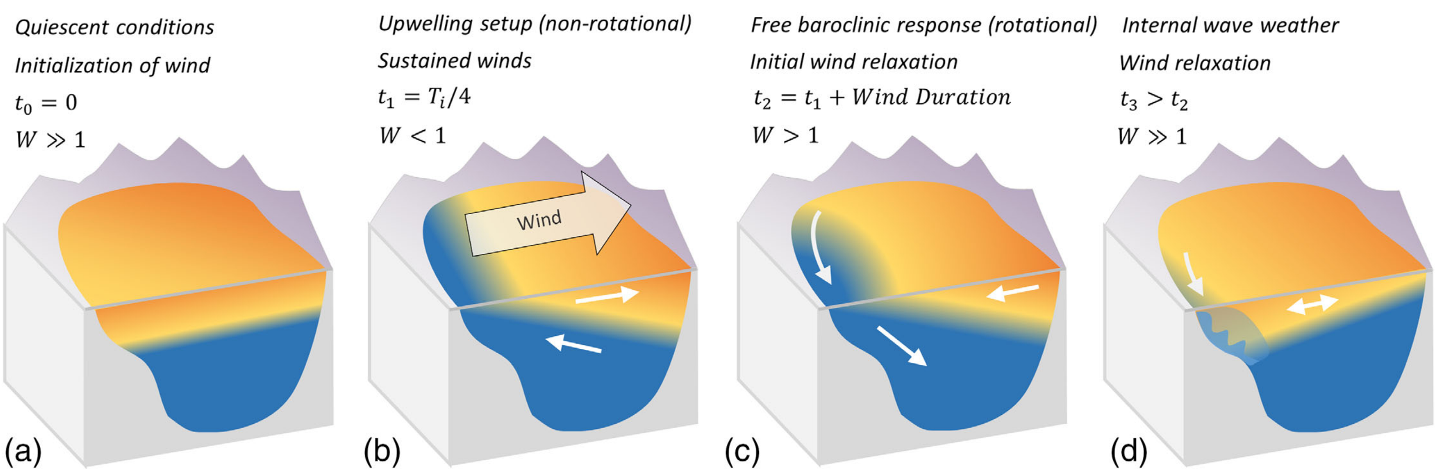

Fig. 12. Schematic of upwelling setup and relaxation in "medium-sized" lakes (as defined in the introduction). (**a**) Stable thermal stratification at initiation of winds. (**b**) Non-rotational upwelling setup (upwind shore upwelling) due to barotropic effect of downwind shore. (**c**) Initialization of rotational internal waves upon relaxation of winds. (**d**) Passage of rotational internal wave fronts and associated boundary mixing. Note that the counter-clockwise currents shown in (**c**) and (**d**) are specific to northern-hemisphere lakes; these fronts would propagate clockwise in southern-hemisphere lakes.

observations in Lake Constance by Lorke et al. (2006). The shallow surface layer depth relative to lake depth (h_1/H) and low values of W are expected to setup conditions conducive to dissipation and mixing as the resulting internal waves interact with the bottom boundary (Horn et al. 2001).

Implications for transport and the relevance of upwelling to nearshore water quality and ecology

The dominant stages associated with upwelling events in medium-sized lakes are illustrated in Fig. 12, which summarizes the sequential steps shown in Figs. 7, 8. The mechanisms by which these events can impact nearshore water quality can be separated into three categories: (1) vertical advection directly associated with upwelling; (2) diapycnal mixing resulting from internal waves/shear stress during upwelling relaxation; and (3) along-shore and cross-shore advection associated with post-upwelling currents and internal waves. In the cases of (1) and (2), water quality impacts are heavily dependent on how vertical concentration gradients in water quality constituents compare with the density profile and magnitude of the wind.

The vertical advection of nutrients and/or Chl *a* concentrations during upwelling is dependent on the magnitude of upwelling relative to the vertical concentration gradients of these water quality constituents (Figs. 7, 9). Transport can thus be predicted as a function of W and pre-event concentration profiles. Though we observed no significant increase in nitrate concentration in the nearshore during our study period, there may have been short-term nitrate increases during E3, as predicted in Figs. 7c, 9b. Under stronger wind conditions, greater isotherm excursions would almost certainly be accompanied by advection of greater nitrate concentrations from depth. While low values of the gradient Richardson number indicate a high degree of shear instability and vertical mixing during upwelling setup (Fig. 8d), these Eulerian observations apply to the cold-water plume advected from depth; mixing within this plume is not indicative of mixing across density-stratified layers. We observed no lasting nitrate increases in the nearshore associated with any of the events despite the (likely) short-term presence of elevated concentrations during these large magnitude upwelling events. To our knowledge, the vertical isotherm excursions observed in Lake Tahoe, described here and in Schladow et al. (2004) as exceeding 70 m, are the largest upwelling magnitudes reported in the limnology literature.

The absence of lasting elevated nitrate concentration in the nearshore postupwelling may be explained by either rapid uptake or downwelling. However, the rise and then rapid drop in nearshore Chl *a* concentration, tracking the pattern predicted by the depth-origin method, seems to point toward rapid downwelling (Fig. 9c). Chl *a* is not a conservative tracer but, unlike nitrate that can be rapidly absorbed by primary producers, the observed rapid decrease (order of hours) is likely indicative of advective transport rather any biological process.

The very large magnitude of the upwelling events but seemingly limited diapycnal mixing are consistent with Vidal et al. (2013) who found that simpler basin shapes (such as Lake Tahoe) lend themselves to greater magnitude upwelling but more limited boundary mixing. Wind relaxation was followed by a period of basin-scale and localized internal waves and currents. Although we did not directly measure turbulent temperature or velocity fluctuations, the observed internal waves and layered flow structure (highlighted in Fig. 8b–d) were likely accompanied by some degree of diapycnal mixing, as indicated by layers of low gradient Richardson numbers in Fig. 8d (after 12:00 on 10 June). Slightly elevated concentrations of nitrate following E3 (Fig. 9b) may be a function of vertical mixing induced by internal wave-driven shear, or to short-lived fluctuations of higher nitrate concentration water due to internal wave dynamics shown in Fig. 6. In any case, we do not expect, nor do we observe, substantial nutrient concentration increases in the nearshore due to diapycnal mixing during upwelling relaxation; nitrate concentrations appear to have been advected to depth, well below the thermocline (see red line in Fig. 9b), prior to the arrival of the most violent, mixing-inducing internal waves (Fig. 8b–d). If nitrate concentrations were to line up more closely with the thermocline, as is often the case in fall at Lake Tahoe, the apparent post-upwelling mixing processes might drive nutrient fluxes into the surface-mixed layer, allowing them to be advected into the littoral zone.

Transport of well-oxygenated surface waters to depth, during upwelling relaxation, may play a role in maintaining hypolimnetic DO concentrations between deep mixing events (Fig. 10). However, it is unclear whether these more oxygenated near-surface waters are transported back to the surface or are diluted into the voluminous hypolimnion.

Dominant along-shore currents, which are governed by the structure of the rotationally influenced internal wave field and likely drive meaningful pore-water flow, could have an effect on the sloughing of periphyton or macrophytes from littoral substrates, and certainly play a role in alongshore transport. Watershed nutrient contributions enter the littoral zone through spatially and temporally variable surface and ground water inputs, leading to localized nearshore primary production (Coats et al. 2008; Naranjo et al. 2019). Internal wave-driven nearshore currents likely induce pore-water exchange (Oldham and Lavery 1999; Cyr 2012) and subsequently advect associated concentrations alongshore. Strong alongshore currents, following upwelling relaxation, would similarly advect inflow concentrations alongshore, potentially to areas typically unaffected by localized inflow loads. Nearshore cooling due to upwelling would render snowmelt inflows near-neutrally buoyant, potentially trapping inflows in the littoral zone (Roberts et al. 2018) and priming their nutrient concentrations to be advected alongshore by the subsequent coastal jet.

Conclusions

Despite significant rotational influence on its internal wave field, upwelling setup in Lake Tahoe more closely follows the non-rotational, closed-basin upwelling pattern than the rotational, coastal upwelling model. The Wedderburn number, W, serves as a reasonable predictor of the timing and spatial extent of upwelling, and as an indicator of the energy associated with the subsequent relaxation.

Observed patterns in upwelling relaxation are consistent with the degree of rotational influence predicted by the Burger number, S (Antenucci and Imberger 2001; de la Fuente et al. 2008), and with previous observations and modeling studies of Lake Tahoe (Rueda et al. 2003). While the strength of stratification and pycnocline depth would seasonally alter the degree of rotational-influence on the post-upwelling internal wave field, we estimate that S never exceeds about 0.85 (assuming peak stratification with $h_1 = 40$ m and average epilimnetic and hypolimnetic temperatures of 20 and 5.5°C, respectively). Lake Tahoe is generally primed to host a suite of rotationally influenced internal wave forms.

Isotherm excursions during upwelling track the vertical transport of nitrate and Chl *a* concentrations from depth. Upwelling magnitudes were rarely sufficient to transport nitrate into the surface waters, but concentrations were observed to increase at mid-depths. Upwelling magnitudes were sufficient to advect Chl *a* concentrations from the deep chlorophyll maximum into the nearshore. Upwelled nitrate and Chl *a* concentrations rapidly decreased to baseline levels after wind relaxation. Since concentrations of these water quality constituents were situated deep relative to the thermocline depth, diapycnal mixing associated with post-upwelling internal wave activity did not appear to drive increased nutrient concentrations into the epilimnion or nearshore. However, in the fall, when the thermocline and nitracline are better aligned, diapycnal mixing during upwelling relaxation may serve as a meaningful nutrient load to the photic zone. Powerful alongshore currents associated with upwelling relaxation likely distribute localized groundwater and inflow nutrient loads through the nearshore. However, the time scale of the events (order of hours) may limit the impact on the littoral ecosystem.

Upwind shore downwelling, during post-upwelling relaxation, drives a downward DO flux at the upwind shore, but it is unclear to what degree oxygen-rich surface waters are mixed into the hypolimnion as the basin-scale waves degenerate. If there is significant mixing, more studies are needed to estimate whether the quantities of oxygen mixed into the hypolimnion play a meaningful role in sustaining near-bottom DO levels.

The findings presented here highlight the complexity of the hydrodynamic processes present at the perimeter of density-stratified, medium-sized lakes. The patterns associated with both upwelling setup and relaxation are recognizable (in comparison to analytical, laboratory, and model results) but can defy expectations when non-dimensional classifications are not interpreted with caution. In lakes generally considered to be rotational, closed-basin effects can limit rotational influence on upwelling setup. However, the resulting internal wave field can still be expected to exhibit rotational characteristics. Despite the fact that the vertical excursions of hypolimnetic water at the upwind shore can be quite large, the currents associated with the resulting rotational internal waves, which arrive at the upwind shore hours after the winds have died down, may be the most vigorous hydrodynamic feature associated with upwelling events. These horizontal currents, rather than upward vertical transport, may also be the most ecologically relevant hydrodynamic feature of upwelling events, particularly when vertical nutrient and oxygen gradients are situated deep relative to vertical density gradients.

References

Antenucci, J. P. 2009. Currents in stratified water bodies 3: Effects of rotation, p. 559–567. *In* G. E. Likens [ed.], Encyclopedia of inland waters, 1st ed. Oxford: Elsevier.

Antenucci, J. P., and J. Imberger. 2001. Energetics of long internal gravity waves in large lakes. Limnol. Oceanogr. **46**: 1760–1773. doi:10.4319/lo.2001.46.7.1760

Antenucci, J. P., J. Imberger, and A. Saggio. 2011. Seasonal evolution of the basin-scale internal lake wave field in a large stratified. **45**: 1621–1638.

Beletsky, D., W. P. O'Connor, D. J. Schwab, and D. E. Dietrich. 1997. Numerical simulation of internal kelvin waves and coastal upwelling fronts. J. Phys. Oceanogr. **27**: 1197–1215.

Bengtsson, L. 1972. Conclusions about turbulent exchange coefficients from model studies. Hydrolog. Sci. Bull. **19**: 306–312. doi:10.1080/02626667409493880

Boegman, L. 2009. Currents in stratified water bodies 2: Internal waves, p. 538–558. *In* G. E. Likens [ed.], Encyclopedia of inland waters, 1st ed. Elsevier.

Boegman, L., G. N. Ivey, and J. Imberger. 2005. The energetics of large-scale internal wave degeneration in lakes. J. Fluid Mech. **531**: 159–180. doi:10.1017/S0022112005003915

Bouffard, D., and U. Lemmin. 2013. Kelvin waves in Lake Geneva. J. Great Lakes Res. **39**: 637–645. doi:10.1016/j.jglr.2013.09.005

Cimatoribus, A. A., U. Lemmin, D. Bouffard, and D. A. Barry. 2018. Nonlinear dynamics of the nearshore boundary layer of a. J. Geophys. Res. Oceans **123**: 1016–1031. doi:10.1002/2017JC013531

Coats, R., M. Larsen, A. Heyvaert, J. Thomas, M. Luck, and J. Reuter. 2008. Nutrient and sediment production, watershed characteristics, and land use in the Tahoe Basin, California-Nevada. J. Am. Water Resour. Assoc. **44**: 754–770. doi:10.1111/j.1752-1688.2008.00203.x

Corman, J. R., P. B. McIntyre, B. Kuboja, W. Mbemba, D. Fink, C. W. Wheeler, C. Gans, E. Michel, and A. S. Flecker. 2010. Upwelling couples chemical and biological dynamics across the littoral and pelagic zones of Lake Tanganyika, East Africa. Limnol. Oceanogr. **55**: 214–224. doi:10.4319/lo.2010.55.1.0214

Csanady, G. T. 1977. Intermittent "full" upwelling in Lake Ontario. J. Geophys. Res. **82**: 397–419. doi:10.1029/JC082i003p00397

Csanady, G. T. 1982. On the structure of transient upwelling events. J. Phys. Oceanogr. **12**: 84–96, doi:10.1175/1520-0485(1982)012<0084:OTSOTU>2.0.CO;2

Cyr, H. 2012. Temperature variability in shallow littoral sediments of Lake Opeongo (Canada). Freshwater Sci. **31**: 895–907. doi:10.1899/11-099.1

De La Fuente, A., K. Shimizu, J. Imberger, and Y. Niño. 2008. The evolution of internal waves in a rotating, stratified, circular basin and the influence of weakly nonlinear and nonhydrostatic accelerations. Limnol. Oceanogr. **53**: 2738–2748. doi:10.4319/lo.2008.53.6.2738

Gill, A. E. 1982. Atmosphere-ocean dynamics. Academic Press.

Gloor, M., A. Wüest, and M. Münnich. 1994. Benthic boundary mixing and resuspension induced by internal seiches. Hydrobiologia **284**: 59–68. doi:10.1007/BF00005731

Grinsted, A., J. C. Moore, and S. Jevrejeva. 2004. Application of the cross wavelet transform and wavelet coherence to geophysical time series. Nonlinear Process. Geophys. **11**: 561–566. doi:10.5194/npg-11-561-2004

Holm-Hansen, O., and B. Riemann. 1978. Chlorophyll *a* determination: Improvements in methodology. Oikos **30**: 438. doi:10.2307/3543338

Horn, D. A., J. Imberger, and G. N. Ivey. 2001. The degeneration of large-scale interfacial gravity waves in lakes. J. Fluid Mech. **434**: 136–207. doi:10.1017/S0022112001003536

Imberger, J., and J. C. Patterson. 1990. Physical limnology, p. 303–475. *In* Advances in applied mechanics. Elsevier.

IOC, SCOR, and IAPSO. 2010. The international thermodynamics equation of seawater—2010: Calculation and use of thermodynamic properties (English). (Int. Oceanogr. Comm. Manuals and Guides No. 56, 196 p.), London, UK: UNESCO.

Kämpf, J. 2015. Interference of wind-driven and pressure gradient-driven flows in shallow homogeneous water bodies. Ocean Dynam. **65**: 1399–1410. doi:10.1007/s10236-015-0882-2

Kamphake, L. J., S. A. Hannah, and J. M. Cohen. 1967. Automated analysis for nitrate by hydrazine reduction. Water Res. **1**: 205–216. doi:10.1016/0043-1354(67)90011-5

Kundu, P. K., I. M. Cohen, and D. R. Dowling. 2012. Fluid mechanics, 5th ed. Oxford, UK: Academic Press, p. 633–635.

Laval, B., J. Morrison, D. J. Potts, E. C. Carmack, S. Vagle, C. James, F. A. McLaughlin, and M. Foreman. 2008. Wind-driven summertime upwelling in a fjord-type lake and its impact on downstream river condition: Quesnel Lake and River, BC, Canada. J. Great Lakes Res. **34**: 189–208.

Leon, L. F., R. E. H. Smith, S. Y. Malkin, D. Depew, M. R. Hipsey, J. P. Antenucci, S. N. Higgins, R. E. Hecky, and R. Y. Rao. 2012. Nested 3D modeling of the spatial dynamics of nutrients and phytoplankton in a Lake Ontario nearshore zone. J. Great Lakes Res. **38**: 171–183. doi:10.1016/j.jglr.2012.02.006

Lorke, A., F. Peeters, and E. Bäuerle. 2006. High-frequency internal waves in the littoral zone of a large lake. Limnol. Oceanogr. **51**(4): 1935–1939. doi:10.4319/lo.2006.51.4.1935

MacIntyre, S., and J. M. Melack. 1995. Vertical and horizontal transport in lakes: Linking littoral, benthic, and pelagic habitats. J. North Am. Benthol. Soc. **14**: 599–615. doi:10.2307/1467544

MacIntyre, S., K. M. Flynn, R. Jellison, and J. R. Romero. 1999. Boundary mixing and nutrient fluxes in Mono Lake, California. Limnol. Oceanogr. **44**: 512–529. doi:10.4319/lo.1999.44.3.0512

MacIntyre, S., and R. Jellison. 2001. Nutrient fluxes from upwelling and enhanced turbulence at the top of the pycnocline in Mono Lake, California. Hydrobiologia **466**: 13–29. doi:10.1023/A:1014563914112

MacIntyre, S., J. F. Clark, R. Jellison, and J. P. Framb. 2009. Turbulent mixing induced by nonlinear internal waves in mono Lake, California. Limnol. Oceanogr. **54**: 2255–2272. doi:10.4319/lo.2009.54.6.2255

Marti, C. L., and J. Imberger. 2008. Exchange between littoral and pelagic waters in a stratified lake due to wind-induced motions: Lake Kinneret, Israel. Hydrobiologia **603**: 25–51. doi:10.1007/s10750-007-9243-6

Monismith, S. 1986. An experimental study of the upwelling response of stratified reservoirs to surface shear stress. J. Fluid Mech. **171**: 407–439. doi:10.1017/S0022112086001507

Monismith, S. G. 1985. Wind-forced motions in stratified lakes and their effect on mixed-layer shear. Limnol. Oceanogr. **30**: 771–783. doi:10.4319/lo.1985.30.4.0771

Monismith, S. G., J. Imberger, and M. L. Morison. 1990. Convective motions in the sidearm of a small reservoir. Source Limnol. Oceanogr. **35**: 1676–1702. doi:10.4319/lo.1990.35.8.1676

Naranjo, R. C., R. G. Niswonger, D. Smith, D. Rosenberry, and S. Chandra. 2019. Linkages between hydrology and seasonal variations of nutrients and periphyton in a large oligotrophic subalpine lake. J. Hydrol. **568**: 877–890. doi:10.1016/j.jhydrol.2018.11.033

Okely, P., and J. Imberger. 2007. Horizontal transport induced by upwelling in a canyon-shaped reservoir. Hydrobiologia **586**: 343–355. doi:10.1007/s10750-007-0706-6

Oldham, C. E., and P. S. Lavery. 1999. Porewater nutrient fluxes in a shallow fetch-limited estuary. Mar. Ecol. Prog. Ser. **183**: 39–47. doi:10.3354/meps183039

Paerl, H. W., R. C. Richards, R. L. Leonard, and C. R. Goldman. 1975. Seasonal nitrate cycling as evidence for complete vertical mixing in Lake Tahoe, California-Nevada1. Limnol. Oceanogr. **20**: 1–8. doi:10.4319/lo.1975.20.1.0001

Plattner, S., D. M. Mason, G. A. Leshkevich, D. J. Schwab, and E. S. Rutherford. 2006. Classifying and forecasting coastal upwellings in Lake Michigan using satellite derived temperature images and buoy data. J. Great Lakes Res. **32**: 63–76, doi:10.3394/0380-1330(2006)32[63:CAFCUI]2.0.CO;2

Pöschke, F., J. Lewandowski, C. Engelhardt, K. Preuß, M. Oczipka, T. Ruhtz, and G. Kirillin. 2015. Upwelling of deep water during thermal stratification onset—A major mechanism of vertical transport in small temperate lakes in spring? Water Resour. Res. **51**: 9612–9627. doi:10.1002/2015WR017579

Rao, Y. R., and D. J. Schwab. 2008. Transport and mixing between the coastal and offshore waters in the Great Lakes: A review. J. Great Lakes Res. **33**: 202–218, doi:10.3394/0380-1330(2007)33[202:tambtc]2.0.co;2

Roberts, D. C., A. L. Forrest, G. B. Sahoo, S. J. Hook, and S. G. Schladow. 2018. Snowmelt timing as a determinant of lake inflow mixing. Water Resour. Res. **54**: 1237–1251. doi:10.1002/2017WR021977

Roberts, D. C., P. Moreno-Casas, F. A. Bombardelli, S. J. Hook, B. R. Hargreaves, and S. G. Schladow. 2019*a*. Predicting wave-induced sediment resuspension at the perimeter of lakes using a steady-state spectral wave model. doi:10.1029/2018WR023742

Roberts, D. C., H. M. Sprague, A. L. Forrest, A. T. Sornborger, S. G. Schladow, and A. L. Forrest. 2019*b*. Observations and modeling of the surface seiches of Lake Tahoe, USA. Aquat. Sci. **81**: (46). doi:10.1007/s00027-019-0644-1

Rueda, F. J., and S. G. Schladow. 2003. Dynamics of large Polymictic Lake. II: Numerical simulations. J. Hydraul. Eng. **129**: 92–101. doi:10.1061/(ASCE)0733-9429(2003)129:2(92)

Rueda, F. J., S. G. Schladow, and S. O. Palmarsson. 2003. Basin-scale internal wave dynamics during a winter cooling period in a large lake. J. Geophys. Res. **108**: 3097. doi:10.1029/2001JC000942

Saggio, A., and J. Imberger. 1998. Internal wave weather in a stratified lake. Limnol. Oceanogr. **43**: 1780–1795. doi:10.4319/lo.1998.43.8.1780

Sahoo, G. B., A. L. Forrest, S. G. Schladow, J. E. Reuter, R. Coats, and M. Dettinger. 2016. Climate change impacts on lake thermal dynamics and ecosystem vulnerabilities. Limnol. Oceanogr. **61**: 496–507. doi:10.1002/lno.10228

Schladow, S. G., S. O. Palmarsson, T. E. Steissberg, S. J. Hook, and F. E. Prata. 2004. An extraordinary upwelling event in a deep thermally stratified lake. Geophys. Res. Lett. **31**: 2–5. doi:10.1029/2004GL020392

Shimizu, K., and J. Imberger. 2008. Energetics and damping of basin-scale internal waves in a strongly stratified lake. Limnol. Oceanogr. **53**: 1574–1588. doi:10.4319/lo.2008.53.4.1574

Shintani, T., A. de la Fuente, Y. Niño, and J. Imberger. 2010. Generalizations of the Wedderburn number: Parameterizing upwelling in stratified lakes. Limnol. Oceanogr. **55**: 1377–1389. doi:10.4319/lo.2010.55.3.1377

Spigel, R. H., and J. Imberger. 1980. The classification of mixed-layer dynamics of lakes of small to medium size. J. Phys. Oceanogr. **10**: 1104–1121, doi:10.1175/1520-0485(1980)010<1104:TCOMLD>2.0.CO;2

Steissberg, T. E., S. J. Hook, and S. G. Schladow. 2005. Characterizing partial upwellings and surface circulation at Lake Tahoe, California-Nevada, USA with thermal infrared images. Remote Sens. Environ. **99**: 2–15. doi:10.1016/j.rse.2005.06.011

Stevens, C., and J. Imberger. 1996. The initial response of a stratified lake to a surface shear stress. J. Fluid Mech. **312**: 39–66. doi:10.1017/S0022112096001917

Stevens, C. L., and G. A. Lawrence. 1997. Estimation of wind-forced internal seiche amplitudes in lakes and reservoirs, with data from British Columbia, Canada. Aquat. Sci. **59**: 115–134. doi:10.1007/BF02523176

Stocker, R., and J. Imberger. 2003. Energy partitioning and horizontal dispersion in a stratified rotating lake. J. Phys. Oceanogr. **33**: 512–529, doi:10.1175/1520-0485(2003)033<0512:EPAHDI>2.0.CO;2

Strayer, D. L., and S. E. G. Findlay. 2010. Ecology of freshwater shore zones. Aquat. Sci. **72**: 127–163. doi:10.1007/s00027-010-0128-9

Strickland, J. D. H., and T. R. Parsons. 1969. A practical handbook of seawater analysis. Fisheries Research Board of Canada Bulletin 167. Q. Rev. Biol. **44**: 327–327. doi:10.1086/406210

Swift, T. J., J. Perez-Losada, S. G. Schladow, J. E. Reuter, A. D. Jassby, and C. R. Goldman. 2006. Water clarity modeling in Lake Tahoe: Linking suspended matter characteristics to Secchi depth. Aquat. Sci. **68**: 1–15. doi:10.1007/s00027-005-0798-x

Thompson, R. O. R. Y., and J. Imberger. 1980. Response of a numerical model of a stratified lake to wind stress, p. 562–570. *In* Proceedings of the 2nd International Symposium for Stratified Flows. Vol. **1**, Trondheim.

Valipour, R., L. F. León, D. Depew, A. Dove, and Y. R. Rao. 2016. High-resolution modeling for development of nearshore ecosystem objectives in eastern Lake Erie. J. Great Lakes Res. **42**: 1241–1251. doi:10.1016/j.jglr.2016.08.011

Valipour, R., Y. R. Rao, L. F. León, and D. Depew. 2019. Nearshore-offshore exchanges in multi-basin coastal waters: Observations and three-dimensional modeling in Lake Erie. J. Great Lakes Res. **45**: 50–60. doi:10.1016/j.jglr.2018.10.005

Vander Zanden, M. J., and Y. Vadeboncoeur. 2020. Putting the lake back together 20 years later: What in the benthos have we learned about habitat linkages in lakes? Inland Waters **0**: 1–17. doi:10.1080/20442041.2020.1712953

Vidal, J., S. MacIntyre, E. E. McPhee-Shaw, W. J. Shaw, and S. G. Monismith. 2013. Temporal and spatial variability of the internal wave field in a lake with complex morphometry. Limnol. Oceanogr. **58**: 1557–1580. doi:10.4319/lo.2013.58.5.1557

Von Schwind, J. J. 1980. Geophysical fluid dynamics for oceanographers. Englewood Cliffs, NJ: Prentice-Hall, p. 128–130.

Walter, R. K., M. Stastna, C. B. Woodson, and S. G. Monismith. 2016. Observations of nonlinear internal waves at a persistent coastal upwelling front. Cont. Shelf Res. **117**: 100–117. doi:10.1016/j.csr.2016.02.007

Wüest, A., and A. Lorke. 2003. Small-scale hydrodynamics in lakes. Annu. Rev. Fluid Mech. **35**: 373–412. doi:10.1146/annurev.fluid.35.101101.161220

Acknowledgments

This material is based upon work supported by a National Science Foundation Graduate Research Fellowship (NSF grant #1650042). Any opinions, findings, and conclusions or recommendations expressed in this material are those of the authors and do not necessarily reflect the views of the National Science Foundation. Support for nearshore water quality stations was provided by the Lahontan Regional Water Quality Control Board and through the philanthropic support of several Lake Tahoe community homeowners. Routine monitoring of nitrate distribution was supported by the Tahoe Regional Planning Agency. Meteorological buoy data were made available by Dr Simon Hook of NASA-JPL. Brant Allen, Katie Senft, Brandon Berry, Raph Townsend, Christine Limon, and Sergio Valbuena of the UC Davis Tahoe Environmental Research Center provided invaluable field and instrumentation support. Robin Roettger of the UC Davis Bodega Marine Lab provided valuable assistance building and organizing moorings. Extensive instrumentation resources were provided by the Stanford Environmental Fluid Mechanics Lab. The authors thank Dr Sally MacIntyre and three anonymous reviewers for their valuable feedback. There are no known conflicts of interest associated with this work. Data associated with this manuscript are available through a UC Davis Library Dryad repository at https://doi.org/10.25338/B8033N. Meteorological data are available from the NASA Jet Propulsion Laboratory at https://laketahoe.jpl.nasa.gov/field-data/.

Conflict of Interest

There are no known conflicts of interest associated with this work.

Submitted 19 July 2019
Revised 17 January 2020
Accepted 14 November 2020

Associate editor: Sally MacIntyre